

6 Applications

A group of tests was defined in order to prove the applicability of the developed tool. This chapter presents the characteristics of the models, as well as the results, comparisons and discussion regarding the advantages and limitations of the implemented code.

In the first part of the Chapter, modelling of laboratory situations is carried out to study the intersections between hydraulic and natural fractures. Four research works mentioned in the literature review (Chapter 2.2.2) are used as basis for the simulation and the published laboratory results are compared with the numerical modelling.

In the second part, a more complex situation is modelled, by considering multiple and intersecting natural fractures in a synthetic model. A sensitivity analysis is also performed in order to understand the effect that two parameters have in the model behaviour.

Finally, a different application is tested. The percolation under a dam foundation is modelled and a comparison with existing results in the literature is made. Additionally, an analysis of the influence that fracture location and aperture may have in the hydraulic behaviour of the foundation is carried out.

6.1. Comparison with laboratory tests

6.1.1. Blanton tests

General description of the simulation

As stated in the Literature Review (Chapter 2.2.2), Blanton (1982) performed a group of laboratory tests, demonstrating the applicability of some analytical formulations to predict what happens when a hydraulic fracture intersects a natural fracture. The research work includes 11 laboratory tests in hydrostone where the natural fracture orientation and the confining stresses vary, with the results shown

in Figure 2.8. In this research, four different natural fracture angles of approach and six different differential stresses are combined, in order to represent the 11 laboratorial tests.

As there is no allusion to conductivity parameters in the reference paper, the hydrostone is considered to be impermeable, i.e., only displacements and fracture pressures are computed.

A qualitative analysis of the results is made, by checking the type of interaction that occurs between fractures and comparing it with the laboratory tests.

Model geometry and mesh

The same geometry is used for all simulations, with a 0,0305 m x 0,0305 m square model divided in a 51x51 element grid. Figure 6.1 shows the mesh used in the analyses with two different orientations for the natural fracture, 60° and 90°. The small circular perforation of the laboratory specimens is represented by a small initial fracture.

Material properties

The material properties are presented in Table 6.1 and Table 6.2. As the samples were created in laboratory, the roughness is expected to be very low, so a value of the initial hydraulic aperture of 1×10^{-6} is adequate. The fracture parameters were not provided by Blanton (1982), so a friction coefficient of 36,9° and cohesionless behaviour are assumed to be suitable. The tangential stiffness before plastification, i.e., for very small relative displacements and high compression stresses, takes the value 1×10^{10} kPa. A non-associated law is used, i.e. no dilatation occurs due to shear deformations.

Initial conditions

The laboratory tests were made applying different combination of confinement pressures so these are also taken into account in the numerical models, by means of a geostatic step. The applied in-situ stresses are presented in Table 6.3. Considering that in every numerical model the propagation is horizontal, the maximum and minimum stresses are applied in the horizontal and vertical directions, respectively.

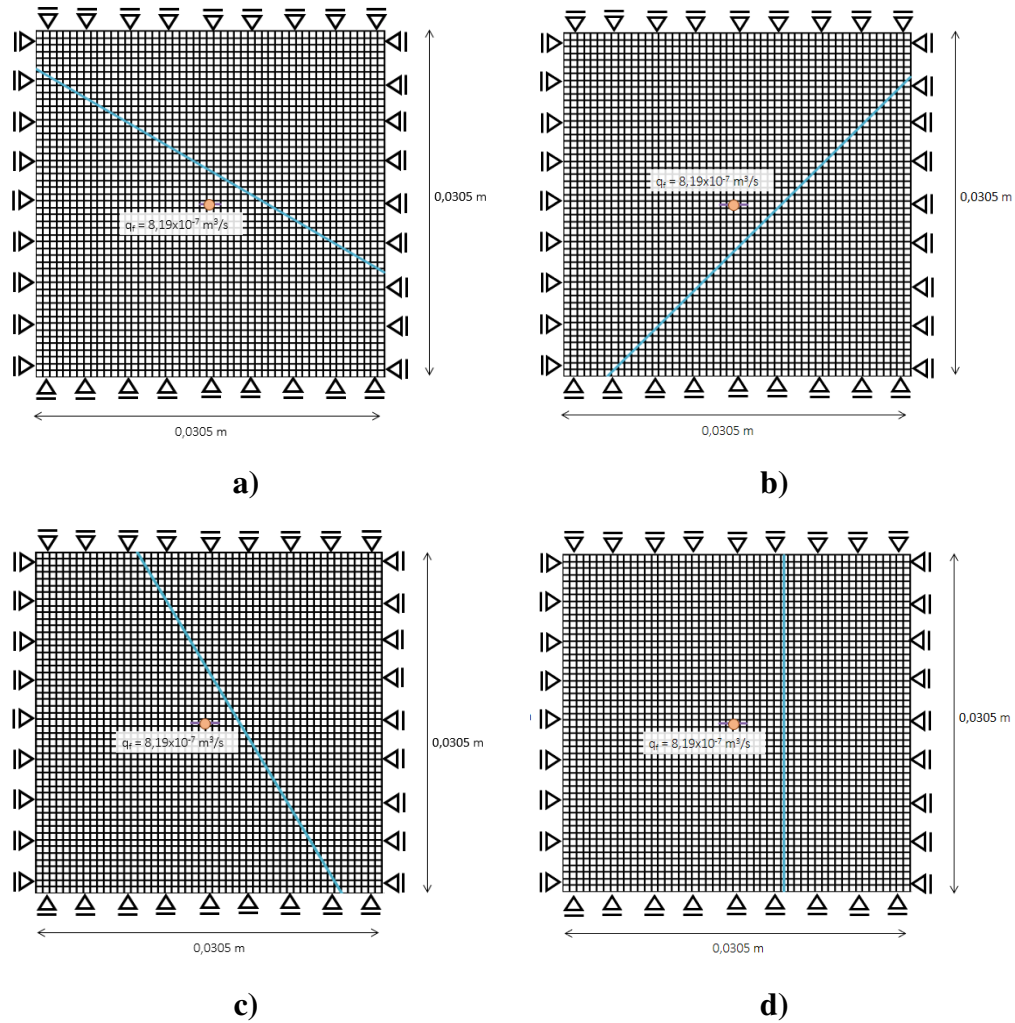


Figure 6.1 – Models used to simulate the different fracture orientations.

a) 30°. b) 45°. c) 60°. d) 90°

Table 6.1 – Hydraulic properties

	Parameter	All Models
Fractures	Initial hydraulic aperture (m)	1×10^{-6} *
	Fluid Viscosity (kPa.s)	10^{-6}

*assumed value

Table 6.2 – Mechanical properties

	Parameter	All Models
Porous Region	E (kPa)	1×10^7
	ν	0,22
	σ_t (kPa)	3100*
Natural Fracture	K_n (kPa)	0**
	K_s (kPa)	1×10^{10} *
	ϕ' (°)	36,9*
	c' (kPa)	0*

*assumed values

**value in traction. In compression, a penalty factor is applied

Table 6.3 – In-situ Stresses

Model	σ_{\max} (kPa)	σ_{\min} (kPa)
4	12×10^3	10×10^3
7	19×10^3	10×10^3
8	20×10^3	5×10^3
9	20×10^3	5×10^3
11	20×10^3	5×10^3
12	18×10^3	5×10^3
13	16×10^3	5×10^3
14	16×10^3	5×10^3
20	14×10^3	5×10^3
21	14×10^3	5×10^3
22	10×10^3	5×10^3

Boundary and loading conditions

The contact with the flatjacks is simulated by displacement fixities and the fluid injection in fracture is defined by a prescribed constant volumetric flux of $8,19 \times 10^{-7} \text{ m}^3/\text{s}$ inside the initial hydraulic fracture.

Once the surrounding material is impermeable, the third pressure activation criterion (see Chapter 4.2.3) is used in the natural fracture. This means that when the simulation starts, the natural fracture has its fracture pressure degrees of

freedom deactivated, so its deformations occur without the influence of the vacuum created by the fracture fluid. Then, when the hydraulic fracture intersects the natural fracture, the segments of the natural fracture with an aperture larger than 2×10^{-7} m have the fracture pressure degrees of freedom activated.

Results

Overall, it may be stated that the numerical procedure provided very good agreement with the laboratory tests. Figure 6.2 presents the intersection behaviour observed in each of the 11 models plotted against the laboratory tests. All models except number 8 predicted the intersection behaviour correctly. As expected, the models with lower angles of approach and differential stresses predict opening, while the model with a perpendicular intersection shows crossing. In all the other simulations with intermediate values of angles and differential stresses, the predicted behaviour is arrest.

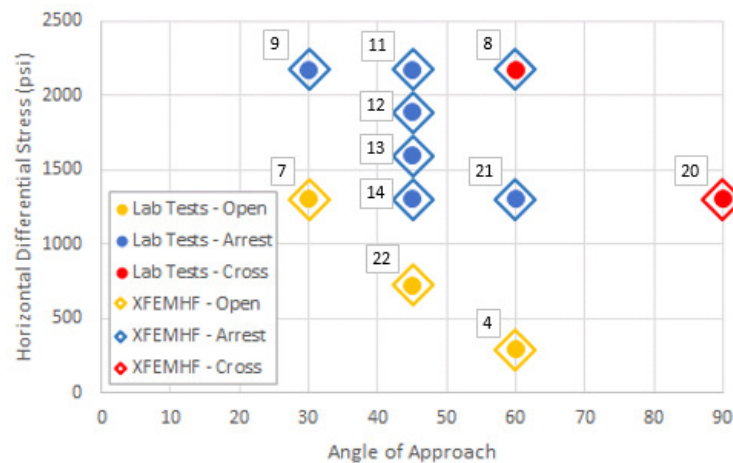


Figure 6.2 – Comparison of the numerical simulations with the laboratory tests numbered according to Blanton (1982)

Figure 6.3 shows the deformed models and compares them with pictures of the available laboratory tests. According to the test photos, the author used the same sample to perform two tests, by rotating the applied confining stresses between tests. Thus, the same sample provided two results for different differential stresses and angles. For the sake of clearness, in some occasions the pictures are rotated in order to match the directions used in the numerical models. Lines are also drawn to highlight the hydraulic fracture paths in each laboratory test.

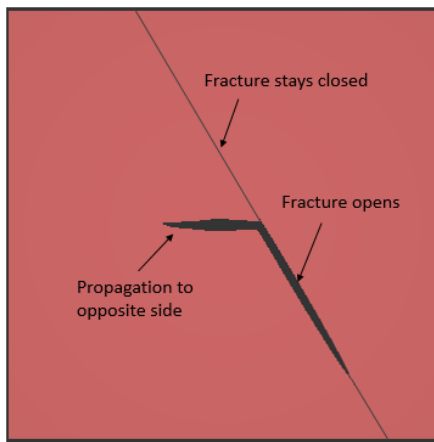
From a more attentive analysis of Figure 6.3 it is noticeable that when opening occurs (models 4, 7 and 22), only half of the pre-existing fracture opens. This is mainly due to the compression that the hydraulic fracture induces in the closer half of the pre-existing fracture. Contrarily, on the other half of the pre-existing fracture tension occurs, leading to its opening. Despite the superposition with the other direction's test, it may be assumed by the picture taken that this occurred in the tests. It should also be noted that when opening events occur the propagation length on the opposite side of the pre-existing fracture tends to be smaller. This is easily understood considering that the fluid is stored in the pre-existing fracture, reducing the pressure inside the hydraulic fracture.

When arrest events occur (models 8, 9, 11, 12, 13, 14 and 21) slight opening may be spotted in the pre-existing fracture. However, the hydraulic fracture is not capable of opening or crossing the pre-existing fracture, propagating instead to the opposite direction. This was also observed by the author, who stated that the opposite fracture wing grew to a greater length and no fluid flow occurred along the pre-existing fracture (Blanton, 1982).

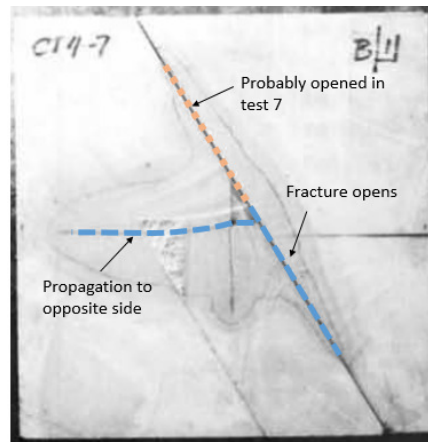
In model 20 crossing takes place and it is visible how the pre-existing fracture almost does not influence the hydraulic fracture behaviour. This is mainly due to the high differential stresses, which result in a high compressive stress in the pre-existing fracture faces. Associated with the high angle of approach of 90° , the entrance of fluid in the pre-existing fracture is highly constrained.

Only one numerical simulation – number 8 – predicted a different intersection type. The main reason for this difference may be related with other parameters that also influence the intersection behaviour. Other researchers have shown that also fracture friction (Hanson, Shaffer and Anderson, 1981), fracture length (Lamont and Jessen, 1963) or viscosity of the injection fluid (Cheng, Jin, Y. Chen, *et al.*, 2014) also influence fracture interaction. Obviously, many other limitations of the model may have led to this result, such as the negligence of dynamic or pore-pressure effects, or even a less realistic computing of the stress at the crack tip due to the use of the signed enrichment function.

Model 4 ($\beta = 60^\circ \parallel \Delta\sigma = 2 \times 10^3$ kPa) – Opening

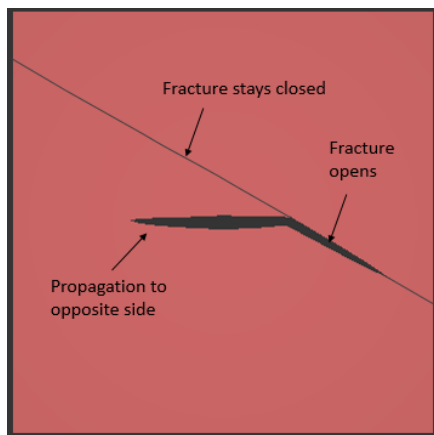


XFEMHF

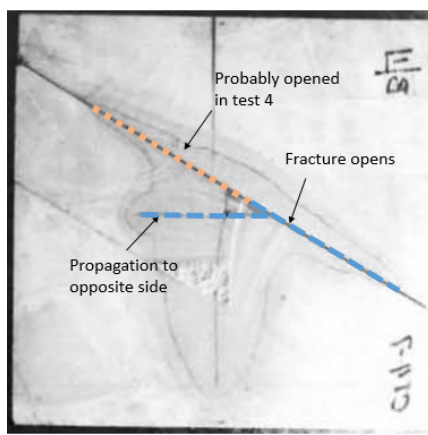


Laboratory Tests

Model 7 ($\beta = 30^\circ \parallel \Delta\sigma = 9 \times 10^3$ kPa) – Opening

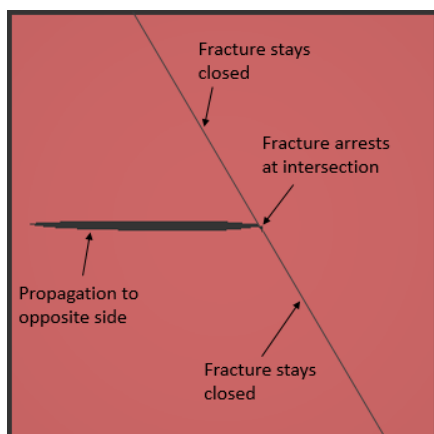


XFEMHF

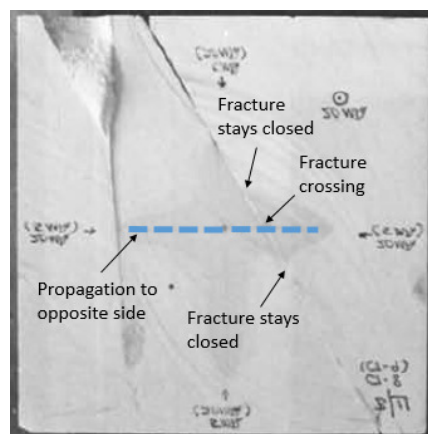


Laboratory Tests

Model 8 ($\beta = 60^\circ \parallel \Delta\sigma = 15 \times 10^3$ kPa) – Arrest (Numerical) or Crossing (Lab)



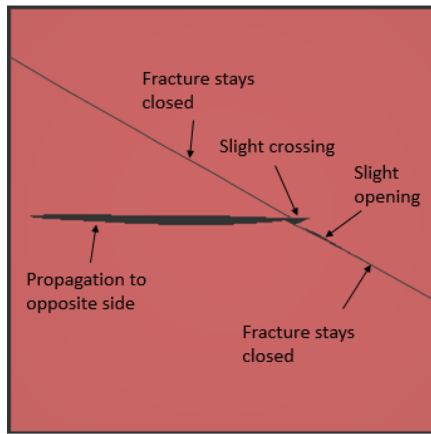
XFEMHF



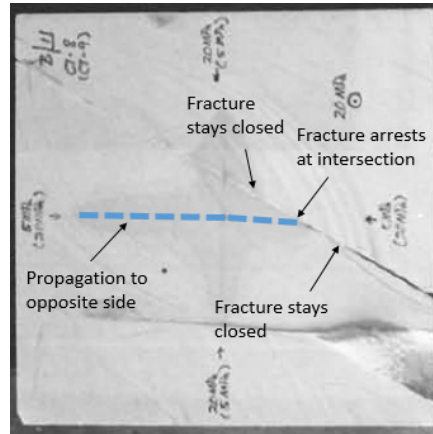
Laboratory Tests

Figure 6.3 – Comparison of deformed models with the laboratory tests (when available)

Model 9 ($\beta = 30^\circ \parallel \Delta\sigma = 15 \times 10^3 \text{ kPa}$) – Arrest

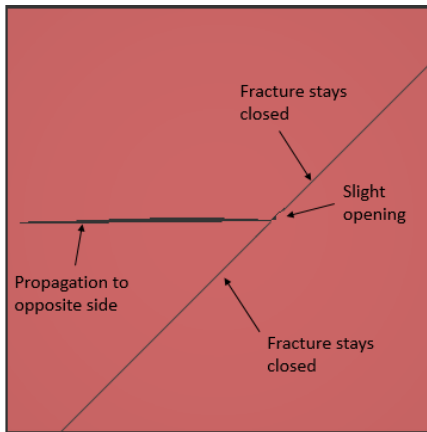


XFEMHF

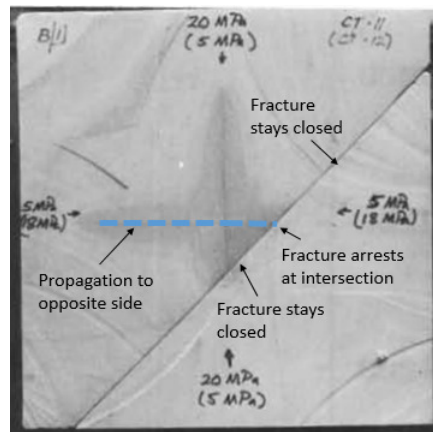


Laboratory Tests

Model 11 ($\beta = 45^\circ \parallel \Delta\sigma = 15 \times 10^3 \text{ kPa}$) – Arrest

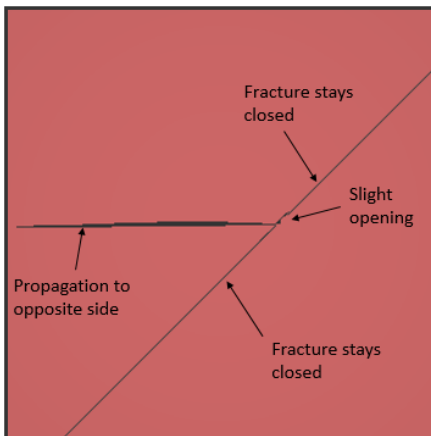


XFEMHF

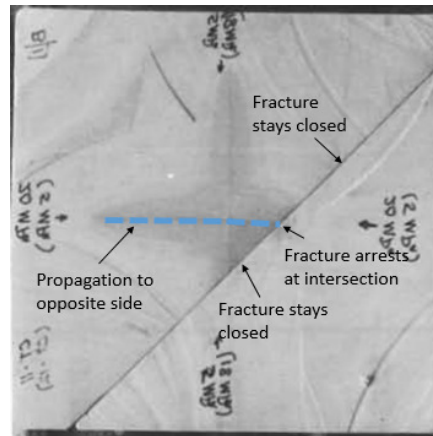


Laboratory Tests

Model 12 ($\beta = 45^\circ \parallel \Delta\sigma = 13 \times 10^3 \text{ kPa}$) – Arrest



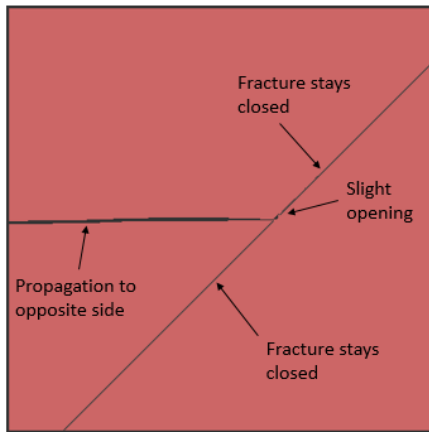
XFEMHF



Laboratory Tests

Figure 6.3 (cont.) – Comparison of deformed models with the laboratory tests (when available)

Model 13 ($\beta = 45^\circ \parallel \Delta\sigma = 11 \times 10^3 \text{ kPa}$) – Arrest

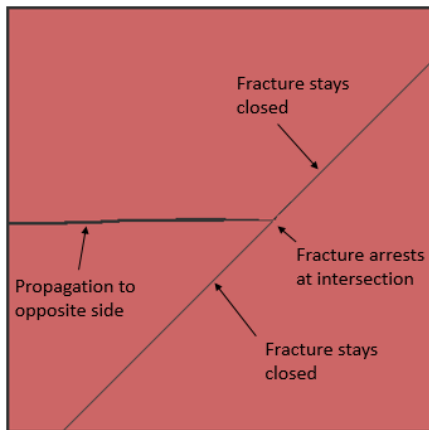


(Not Available)

XFEMHF

Laboratory Tests

Model 14 ($\beta = 45^\circ \parallel \Delta\sigma = 9 \times 10^3 \text{ kPa}$) – Arrest

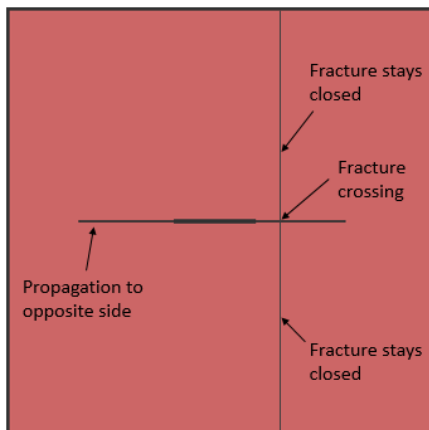


(Not Available)

XFEMHF

Laboratory Tests

Model 20 ($\beta = 90^\circ \parallel \Delta\sigma = 9 \times 10^3 \text{ kPa}$) – Crossing

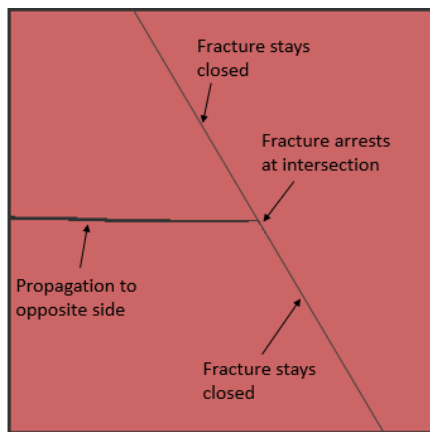


(Not Available)

XFEMHF

Laboratory Tests

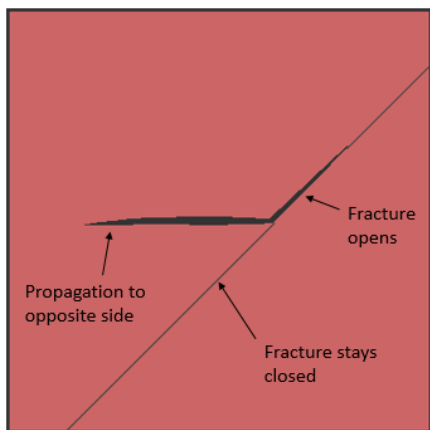
Figure 6.3 (cont.) – Comparison of deformed models with the laboratory tests (when available)

Model 21 ($\beta = 60^\circ \parallel \Delta\sigma = 9 \times 10^3 \text{ kPa}$) – Arrest

(Not Available)

XFEMHF

Laboratory Tests

Model 22 ($\beta = 45^\circ \parallel \Delta\sigma = 5 \times 10^3 \text{ kPa}$) – Opening

(Not Available)

XFEMHF

Laboratory Tests

Figure 6.3 (cont.) – Comparison of deformed models with the laboratory tests (when available)

The output of fracture variables allows a better knowledge of the behaviour of the existing fracture around the intersection. By plotting the relative shear (shear stress divided by the shear strength) along the pre-existing fracture for model 22, as seen in Figure 6.4, it is clear that the closer to the intersection, the higher is the relative shear acting in the faces. In the first presented time increment ($t = 0,06 \text{ s}$), the high compression under the hydraulic fracture increases the shear strength, therefore decreasing the relative shear. As intersection occurs ($t = 0,07 \text{ s}$), the flow enters the pre-existing fracture and a reduction of the horizontal fracture aperture happens. This brings a rapid reduction of the effect of the hydraulic fracture in the pre-existing fracture, i.e., a decrease of the compression in the region under the hydraulic fracture that leads to an increase of the relative shear and a reduction of

the tensile forces in the region above the hydraulic fracture that leads to a decrease of the relative shear. As the fluid enters the pre-existing fracture (t = 0,09 s and t = 0,11 s), the fracture faces lose contact and the shear strength is lost (relative shear of 100%). Then, the fluid has more and more impact in separating and pressurizing the fracture faces, continuing the opening event.

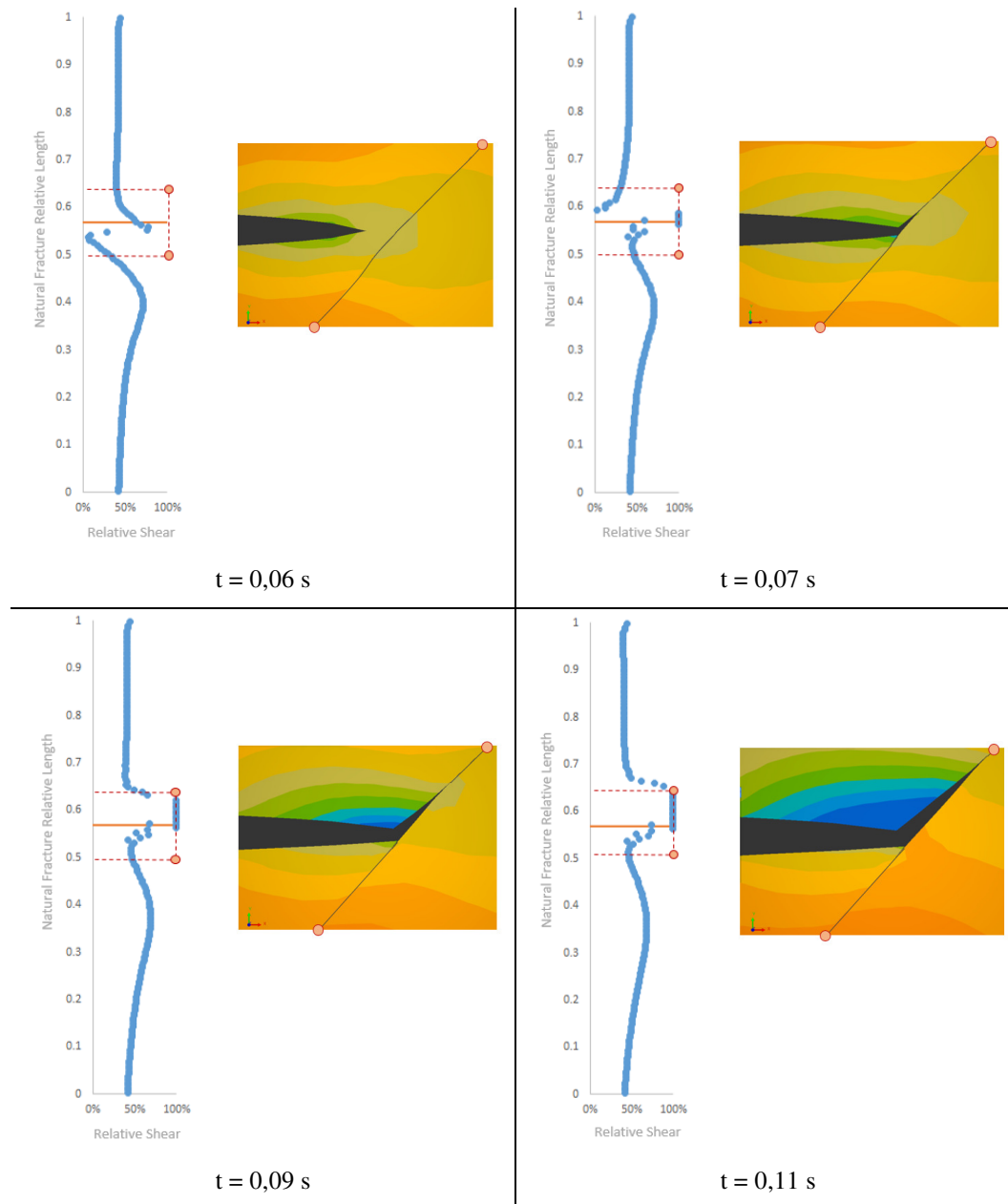


Figure 6.4 – Relative shear stresses in the pre-existing fracture for model 22. Red dashed lines denote the extremities of the fracture represented in the near figure. Orange line represents the level of the intersection.

A similar analysis, yet with different results, may be done to model 20 (see Figure 6.5). Naturally, the region closer to the intersection is subjected to higher

relative shears. Until the hydraulic fracture reaches the pre-existing fracture, the relative shears are very low, as seen in the increment previous to the intersection ($t = 0,07$ s). As the compression in the fracture faces is high, the strength increases and the transmission of shear stresses between the fracture faces generate tensile stresses on the opposite side. Consequently, the tensile strength is reached on the across the pre-existing fracture and the hydraulic fracture continues to propagate.

When the intersection occurs ($t = 0,08$ s), there is a sudden increase of the relative shears, but only the closest points to the intersection reach the shear strength and failure. The rest of the fracture keeps a compressive state, which does not allow the penetration of fluid in the pre-existing fracture. Then, as the hydraulic fracture moves away from the intersection ($t = 0,09$ s and $t = 0,12$ s), the displacements due to hydraulic fracture tend to be similar in both sides of the pre-existing fracture, reducing the shear stresses.

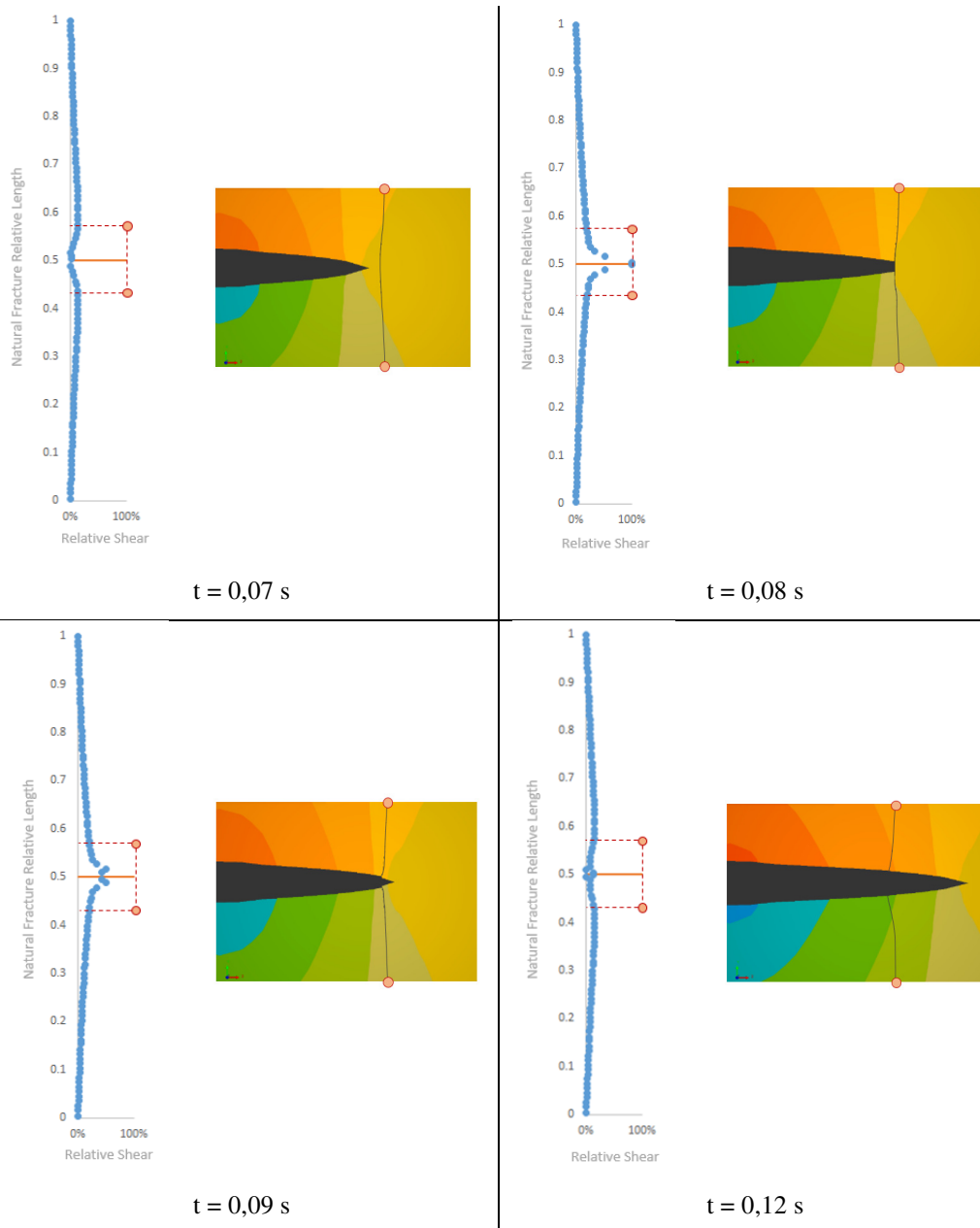


Figure 6.5 – Relative shear stresses in the pre-existing fracture for model 20. Red dashed lines denote the extremities of the fracture represented in the near figure. Orange line represents the level of the intersection.

6.1.2. Khoei tests

General description of the simulation

Khoi *et al.* (2015) performed hydraulic fracturing laboratory tests in two naturally fractured nearly impermeable carbonate rock samples. Moreover, the authors compared the laboratory tests with numerical simulations using the XFEM

technique. In this section, the simulation of the two laboratory tests is performed and compared with both the laboratory and numerical results of Khoei *et al.* (2015).

As referred by Khoei *et al.* (2015), the rock is considered to be impermeable, i.e., only displacements and fracture pressures are computed. A qualitative analysis of the results is made, by checking the type of interaction that occurs between fractures and comparing it with the laboratory tests.

Model geometry and mesh

Two models are defined to match the laboratory specimens' dimensions. Figure 6.6 shows a schematic representation of the models and Figure 6.7 the meshes used in the analyses. Table 6.4 indicates the dimensions of the models and the coordinates of the initial notch and the natural fracture.

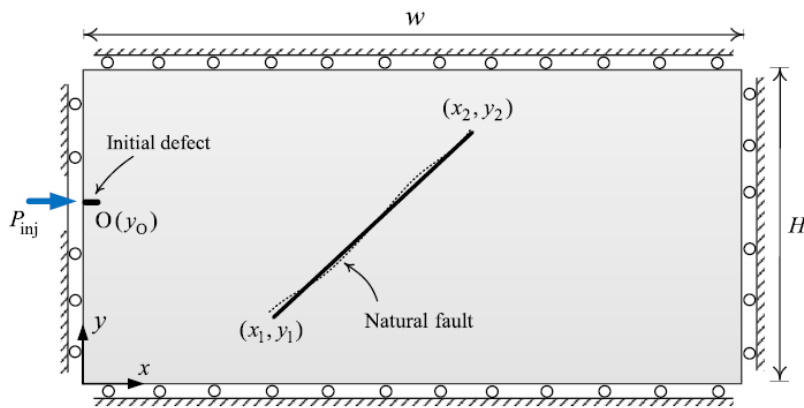
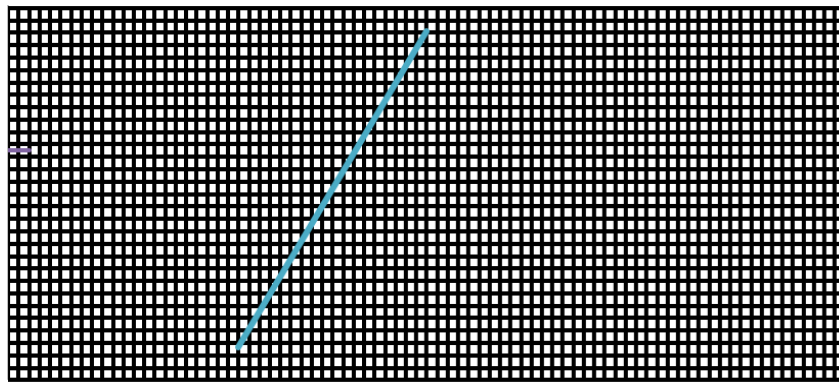
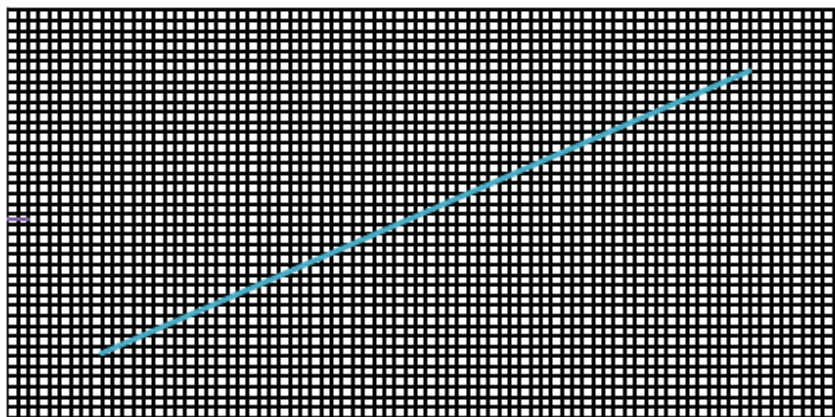


Figure 6.6 – Schematic view of the geometry and boundary conditions of hydraulic fracturing experimental tests



a)



b)

Figure 6.7 – Meshes used in the simulations. a) Specimen 1. b) Specimen 2

Table 6.4 – Geometry and material properties of the two hydraulic fracturing experiments

	Width (mm)	Height (mm)	(x₁,y₁) (mm)	(x₂,y₂) (mm)	y₀ (mm)
Specimen 1	111	45	(30,5;4)	(55,4;42,16)	27,9
Specimen 2	110	54	(12,13;8,82)	(98,12;46,07)	26,9

Material properties

The material properties are presented in Table 6.8 and Table 6.6. Some parameters were not provided in the reference paper, so values based in accumulated experience with rocks were assumed. It must be noted that the tensile strength values provided in the reference are considered to be much higher than acceptable values for rocks. Therefore, a value for the tensile strength was also assumed in these simulations.

Table 6.5 – Hydraulic properties

	Parameter	All Models
Fractures	Initial hydraulic aperture (m)	5×10^{-5} *
	Fluid Viscosity (kPa.s)	10^{-6} *

*assumed value

Table 6.6 – Mechanical properties

	Parameter	Specimen 1	Specimen 2
Porous Region	E (kPa)	$36,5 \times 10^6$	$32,5 \times 10^6$
	ν	0,25	0,25
	σ_t (kPa)	6000*	6000*
Natural Fracture	K_n (kPa)	0**	0**
	K_s (kPa)	1×10^9 *	1×10^9 *
	ϕ' (°)	36,7	36,7
	c' (kPa)	0	0

*assumed values

**value in traction. In compression, a penalty factor is applied

Boundary and loading conditions

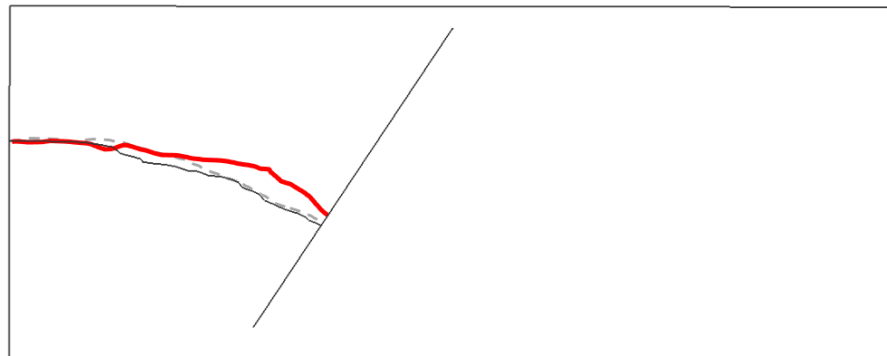
The contact test apparatus is simulated by displacement fixities and the fluid injection in fracture is defined by a prescribed constant pressure of 39300 kPa inside the initial hydraulic fracture.

Once the surrounding material is impermeable and the confinement level is low, i.e. there are no initial stresses applied in the model, the first pressure activation criterion (see Chapter 4.2.3) is used in the natural fracture. This means that when the simulation starts, the natural fracture has its fracture pressure degrees of freedom deactivated, so its deformations occur without the influence of the vacuum created by the fracture fluid. Then, when the hydraulic fracture intersects the natural fracture, all the segments of the natural fracture have their fracture pressure degrees of freedom activated.

Results

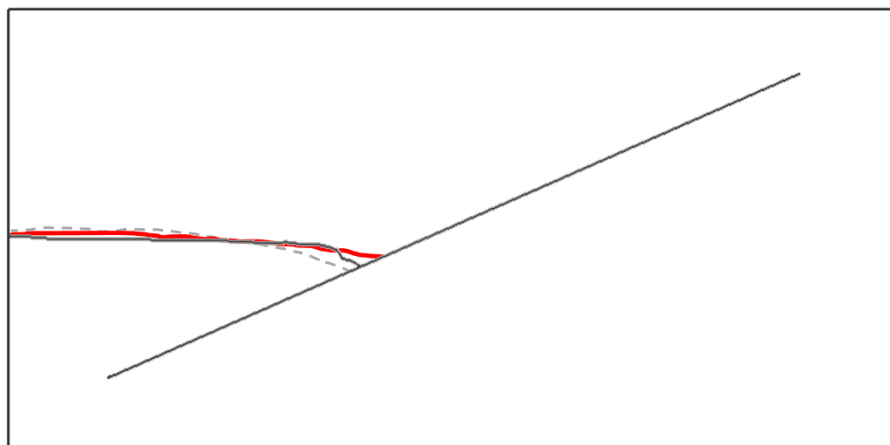
Figure 6.8 shows the crack trajectories obtained in the laboratory tests and numerical simulations with XFEMHF and by Khoei *et al.* (2015). The numerical

simulation trajectories obtained for both specimens are in very good agreement with the laboratory trajectories. Effects that are not taken into account in the numerical simulations, such as the heterogeneity of the material, may explain the slight differences in the comparison with the laboratory tests. It is easily noticeable how the presence of the natural fracture affects the hydraulic fracture trajectory, which has tendency to curve so the junction between fractures occurs closer to perpendicular.



— XFEMHF — Lab. Test (Khoei et al 2015) - - - Numerical (Khoei et al 2015)

a)



— XFEMHF — Lab. Test (Khoei et al 2015) - - - Numerical (Khoei et al 2015)

b)

Figure 6.8 – Comparison of crack trajectory between the numerical solution with XFEMHF, laboratory test and numerical solution by Khoei *et al.* (2015). a) Specimen 1. b) Specimen 2

Figure 6.9 presents the displacement fields in both numerical analyses, XFEMHF and the one presented by Khoei *et al.* (2015). As stated before, Khoei *et al.* (2015) used the XFEM and a very similar formulation to perform the

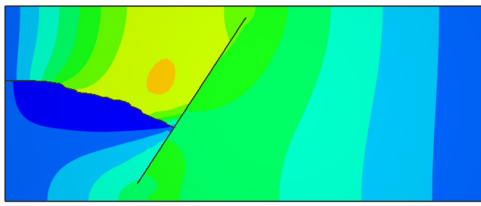
simulations. However, it must be noted that slight differences that exist between the formulations and the implementations applied in each research work may explain the differences in the numerical results. It is known that the tip enrichments are different, and so are the criteria involved with propagation. Therefore, the comparison between numerical tools is carried out more in a qualitative perspective than quantitative. From that viewpoint, it is noticeable how the displacement fields show similar tendencies.

The same qualitative analysis may be performed by comparing the aperture and normal stress profiles along the natural fracture in three different phases of the analysis, defined by the length of the hydraulic fracture L_f . Figure 6.10 and Figure 6.11 compare the results between research works. Despite slight differences in the values, the shape and the development in time show a very good agreement between simulations. In both specimen simulation is noticeable that as the hydraulic fracture approaches the natural fracture, the latter tends to open at its mid-length, where the hydraulic fracture is closer. Moreover, the contact stress in the region farther to the contact increases, due to the displacements that occur in the hydraulic fracture.

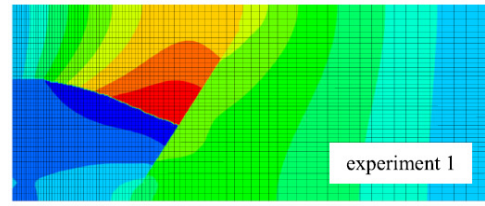
Comparing the two specimens, the different natural fracture inclinations show that, the more vertical is the natural fracture (specimen 1), the more symmetric is the normal stress increase in its extremities. On the other hand, a lower angle of approach (specimen 2) show that the compressive stresses in the lower part of the natural fracture are much higher, while the variations in the upper part are almost none.

Finally, Figure 6.12 presents the plots for two different time increments of the maximum principal stress at the right side of the natural fracture, i.e. at the opposite side of the hydraulic fracture. It is visible that the results obtained with XFEMHF are much smoother than the ones obtained by Khoei *et al.* (2015). However, the same tendency is patent, showing that an increase of the maximum principal stress occurs closer to the junction and at the natural fracture tips as the hydraulic fracture approaches. This shows how the presence of a hydraulic fracture increases the chances of propagation from the natural fracture, both from its tips or the junction.

Specimen 1 – Horizontal displacements



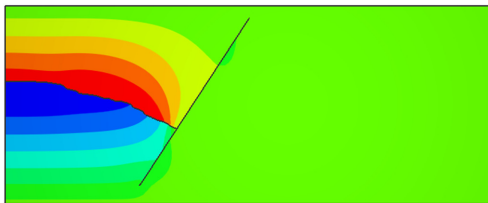
XFEMHF



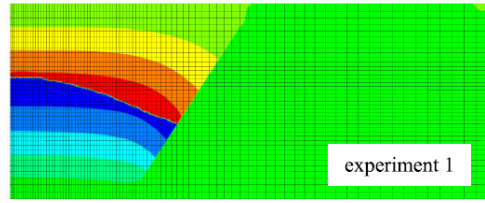
experiment 1

Displacement u_x -0.002 0.016Khoei *et al.*

Specimen 1 – Vertical displacements



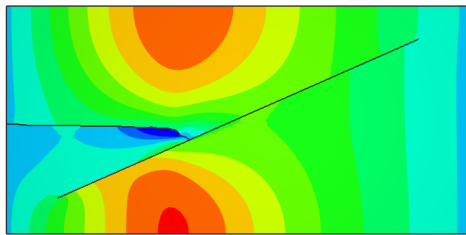
XFEMHF



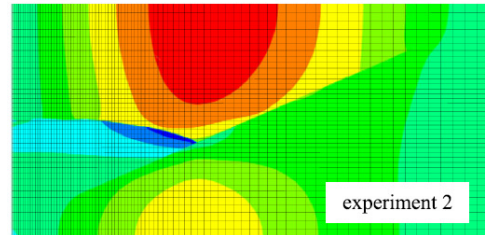
experiment 1

Displacement u_y -0.02 0.015Khoei *et al.*

Specimen 2 – Horizontal displacements



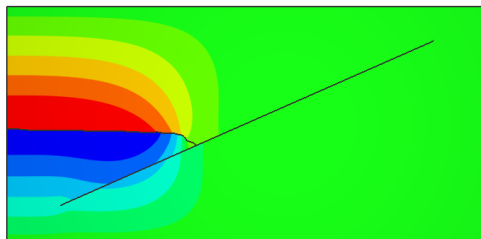
XFEMHF



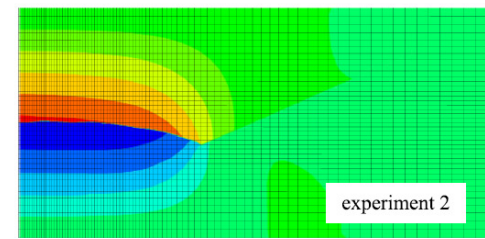
experiment 2

Displacement u_x -0.004 0.012Khoei *et al.*

Specimen 2 – Vertical displacements



XFEMHF

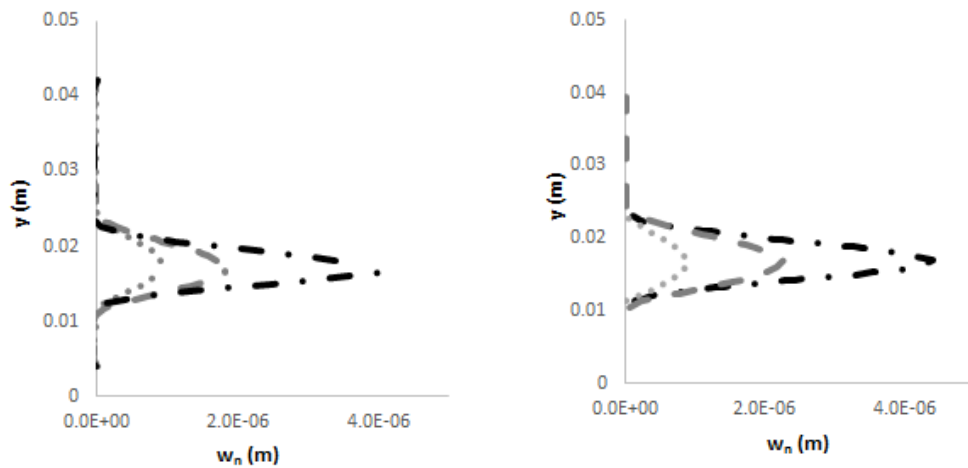


experiment 2

Displacement u_y -0.025 0.025Khoei *et al.*

Figure 6.9 – Comparison of displacement fields when junction occurs between numerical solutions (the same colour scale is used in both simulations)

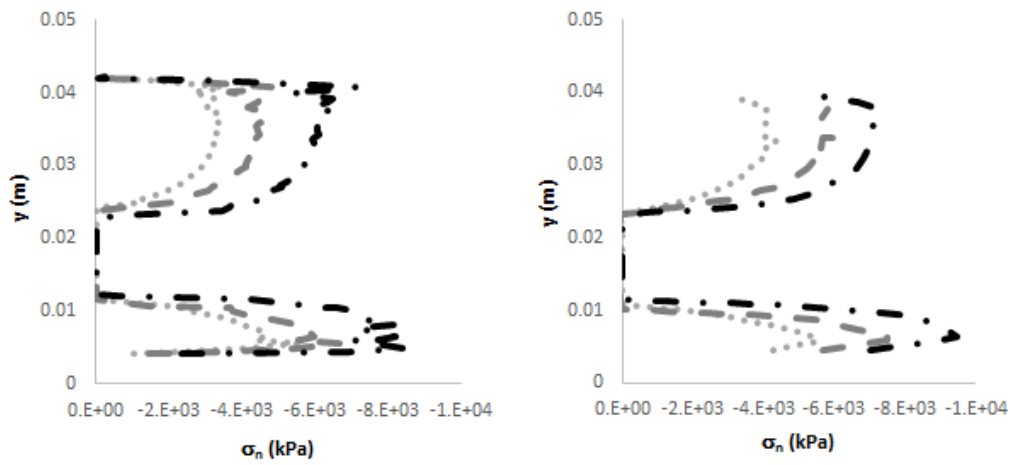
Specimen 1 – Natural fracture aperture



XFEMHF

Khoei *et al.*

Specimen 1 – Natural fracture normal stress



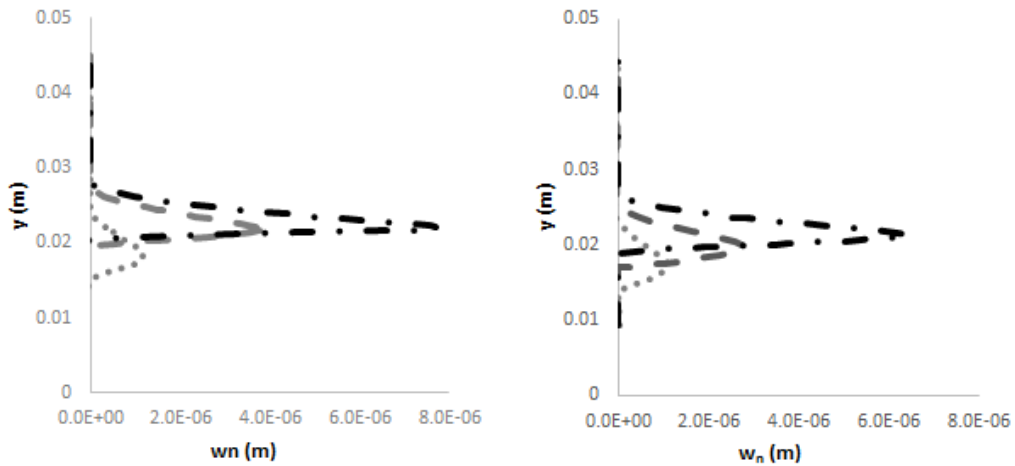
XFEMHF

Khoei *et al.*

..... $L_f = 26,10$ mm - - - - $L_f = 30,96$ mm - . - . - $L_f = 36,15$ mm

Figure 6.10 – Comparison of fracture aperture and normal stress along the natural fracture between numerical solutions for specimen 1

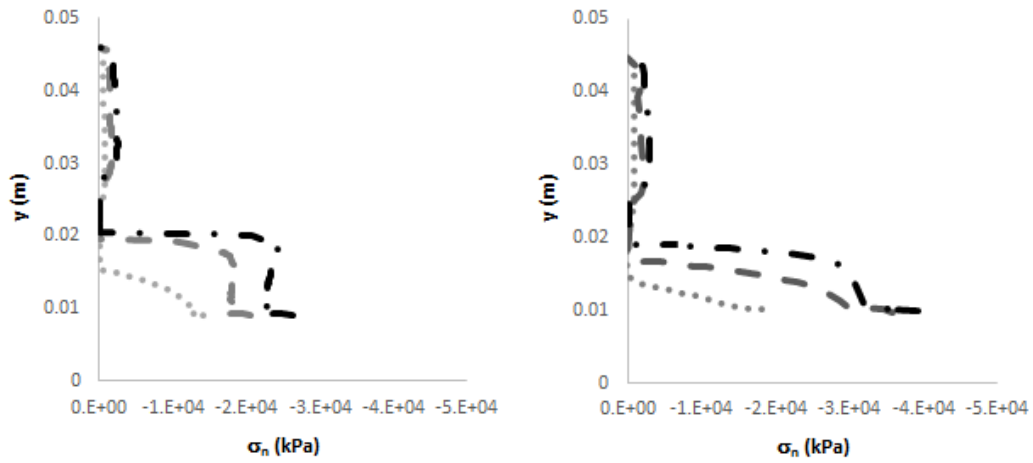
Specimen 2 – Natural fracture aperture



XFEMHF

Khoi *et al.*

Specimen 2 – Natural fracture normal stress



XFEMHF

Khoi *et al.*

..... $L_f = 18,59$ mm - - - - $L_f = 30,68$ mm - · - · - $L_f = 38,90$ mm

Figure 6.11 – Comparison of fracture aperture and normal stress along the natural fracture between numerical solutions for specimen 2

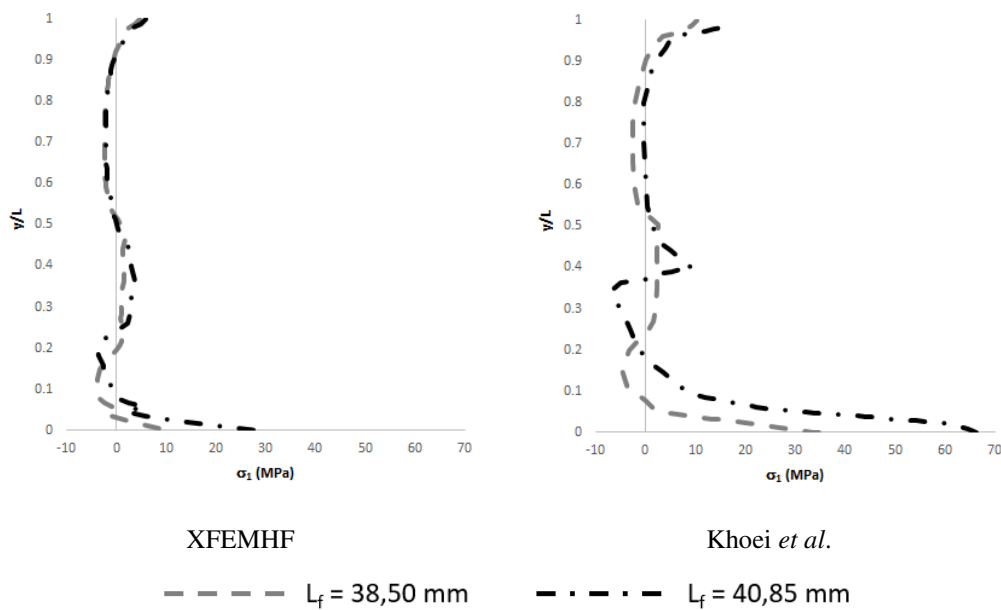
Specimen 1 – Maximum principal stress σ_1 at the right side of the natural fracture

Figure 6.12 – Comparison between numerical solutions for specimen 1 of maximum principal stress σ_1 at the right side of the natural fault

6.2. Propagation of hydraulic fracture in multi-fractured medium

General description of the simulation

The simulations presented in Chapter 6.1 show how to use the developed research in understanding the behaviour of the intersection between one hydraulic fracture and one natural fracture. However, the implementation is generalized for any number of fractures and fracture intersections. Therefore, it is relevant to go further and apply the XFEMHF code in simulations where more fractures and intersections occur.

To the knowledge of the author, no clear information on laboratory tests or numerical simulations of hydraulic fractures propagating in a multi-fractured porous medium exists. Therefore, this work proposes a synthetic model of propagation in a multi-fractured medium.

The model's geometry is defined and a sensibility analysis is performed by changing two parameters, setting a combination of thirty different simulations to be run. The changed parameters are the differential in-situ stress and the in-situ fracture aperture. The sensibility of the created fracture network to each of the varying parameters is analysed in the results.

Additionally, a qualitative comparison is made with the conclusions presented by Zhou and Xue (2011). In their research work, Zhou and Xue (2011) performed hydraulic fracturing laboratory tests in cement blocks that were previously subjected to heat and cooling, in order to form natural fractures inside the blocks. By performing the injections at different differential stresses, the authors found that these influence the fracture network patterns, as Figure 6.13 shows. Three types of geometries were observed in the laboratory tests. The first is a vertical dominating fracture with multiple branches, which was created at high difference stresses, with the dominating fracture still propagating close to the preferred direction, i.e. the direction of maximum stress. The second is a radial net-fracture geometry around the wellbore, which occurs for low stress difference. The third is a partly vertical fracture with random branches for intermediate values of stress difference. Figure 6.14 shows a plot of the results for each test against the differential in-situ stresses. The results show that the higher the differential in-situ stresses, the less the natural fractures affect the hydraulic fracture path.



Figure 6.13 – Fracture patterns obtained in different tests. a) Dominating fracture with multiple branches at large difference of horizontal stress. b) Radial random net-fractures at low difference of horizontal stress (Zhou and Xue, 2011)

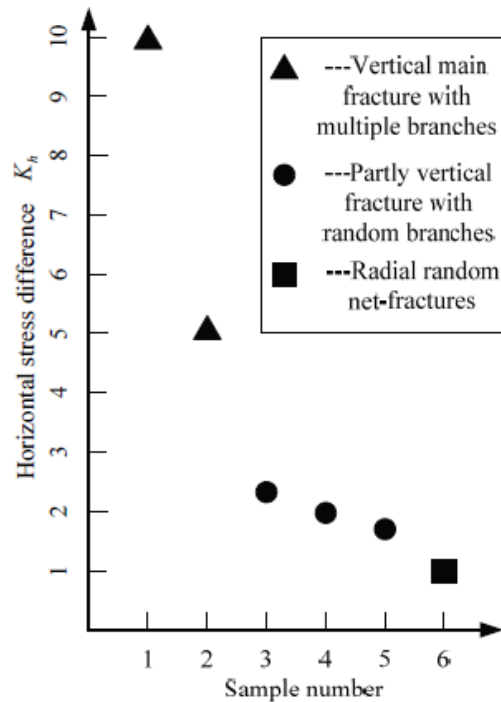


Figure 6.14 – The relation between fracture geometry and in-situ stress contrast (Zhou and Xue, 2011)

Model geometry and mesh

All simulations use a 2,0 m x 1,5 m rectangular model divided in a 75x51 regular element grid. Figure 6.15 shows one initial hydraulic fracture and 9 natural fractures that are placed in a way that two sets of natural fractures are represented with inclinations of 81° (sub-vertical) and -14° (sub-horizontal). The natural fractures are positioned so 5 intersections occur.

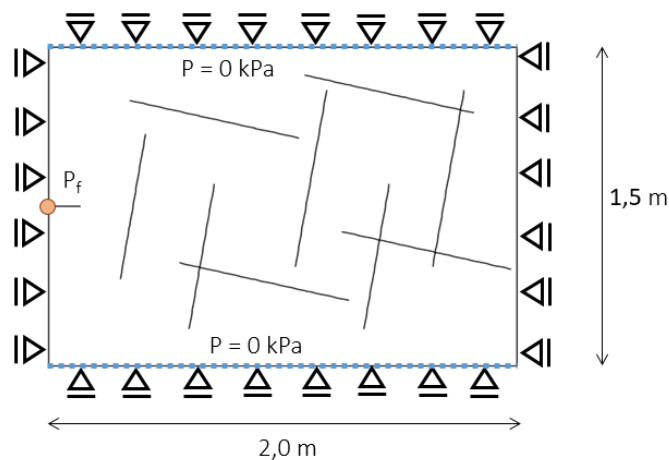


Figure 6.15 – Geometry of the model and boundary conditions.

Material properties

Table 6.7 and Table 6.8 present the fixed parameters chosen for the materials. Although assumed, it is judged that the parameters are within a range of representing correctly a typical fractured rock medium. As for the fracture mechanical behaviour, a non-associated law is used, i.e. no dilatation occurs due to shear deformations.

Table 6.7 – Hydraulic properties

	Parameter	All Cases
Porous Region	Hydraulic conductivity: $k = k_x = k_y$ (m/s)	10^{-11}
Fractures	Fracture face transversal conductivity: $c = c_{top} = c_{bottom}$ (m/s.kPa ⁻¹)	10^{-3}
	Fluid Viscosity (kPa.s)	10^{-6}

Table 6.8 – Mechanical properties

	Parameter	All Cases
Porous Region	E (kPa)	1×10^7
	ν	0,22
	σ_t (kPa)	1100
Natural Fractures	K_n (kPa)	0**
	K_s (kPa)	10^8
	ϕ' (°)	36,9
	c' (kPa)	0

**value in traction. In compression, a penalty factor is applied

Variable properties

The sensibility analysis is performed by varying the in-situ hydraulic fracture aperture and the in-situ stresses. The in-situ hydraulic fracture aperture varies

within three values: 1×10^{-6} , 5×10^{-5} , 5×10^{-4} m. The maximum and minimum value of in-situ hydraulic fracture aperture, 5×10^{-4} and 1×10^{-6} m, respectively, are thought to be representative of limit values for fracture aperture. Those orders of magnitude agree with the range of values studied by Witherspoon *et al.* (1980), who validated the cubic law for use in fracture flow of rock samples subjected to in-situ stresses up to 20 MPa with apertures between $2,5 \times 10^{-4}$ and 4×10^{-6} m.

A geostatic step is used to apply ten different combinations of initial stresses with the values presented in Table 6.9. The maximum and minimum stresses are applied in the horizontal and vertical directions, respectively. The maximum in-situ stress is kept with a constant value of 5×10^3 kPa while the minimum in-situ stress varies between 5×10^3 and $0,312 \times 10^3$ kPa. A dimensionless parameter K_h is used to indicate the relation between maximum and minimum in-situ stresses.

Table 6.9 – In-situ Stresses

σ_{max} (kPa)	σ_{min} (kPa)	$K_h = \frac{\sigma_{max} - \sigma_{min}}{\sigma_{min}}$
5×10^3	5×10^3	0
5×10^3	$4,545 \times 10^3$	0,1
5×10^3	$2,5 \times 10^3$	1
5×10^3	$2,0 \times 10^3$	1,5
5×10^3	$1,428 \times 10^3$	2,5
5×10^3	$1,0 \times 10^3$	4
5×10^3	$0,769 \times 10^3$	5,5
5×10^3	$0,625 \times 10^3$	7
5×10^3	$0,454 \times 10^3$	10
5×10^3	$0,312 \times 10^3$	15

Boundary and loading conditions

Along the whole model border the displacements are fixed perpendicularly to it, as seen in Figure 6.15. To allow the flow of fluid outside the model, the pressure at the top and bottom borders is fixed.

The simulations are set to run one single step of 100 s with increment time limited to a maximum of 2 s. Fluid injection in the hydraulic fracture is given by an imposed fracture pressure that follows the ramp function $P_f = 2000 \cdot t$, as presented in Figure 6.16.

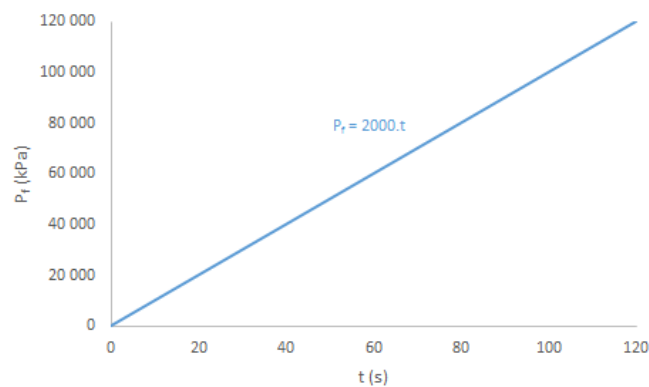


Figure 6.16 – Fluid Pressure applied at the hydraulic fracture mouth

Results

The results show that the implemented code is capable of simulating the propagation of a hydraulic fracture in a multi-fractured medium. It may be stated that the created fracture networks are highly dependent on the parameters that varied. Figure 6.17 shows the deformed geometry and the pore pressure fields for three calculations with very different in-situ stress relations. It is evident that as the stress parameter K_h increases, the events of fracture opening are less likening to occur and the hydraulic fracture tends to cross the natural fractures. For a low value of K_h , opening occurs in the natural fractures and their tips propagate until reaching other natural fractures.

The pore-pressure fields indicate that the pattern of pore-pressures is strongly affected by the leak-off in the fractures. For higher values of K_h , higher pore-pressures concentrate close to the hydraulic fracture. On the other hand, for lower values of K_h , the higher-pressure regions are much more dependent on the natural fractures position and depend on their communication.

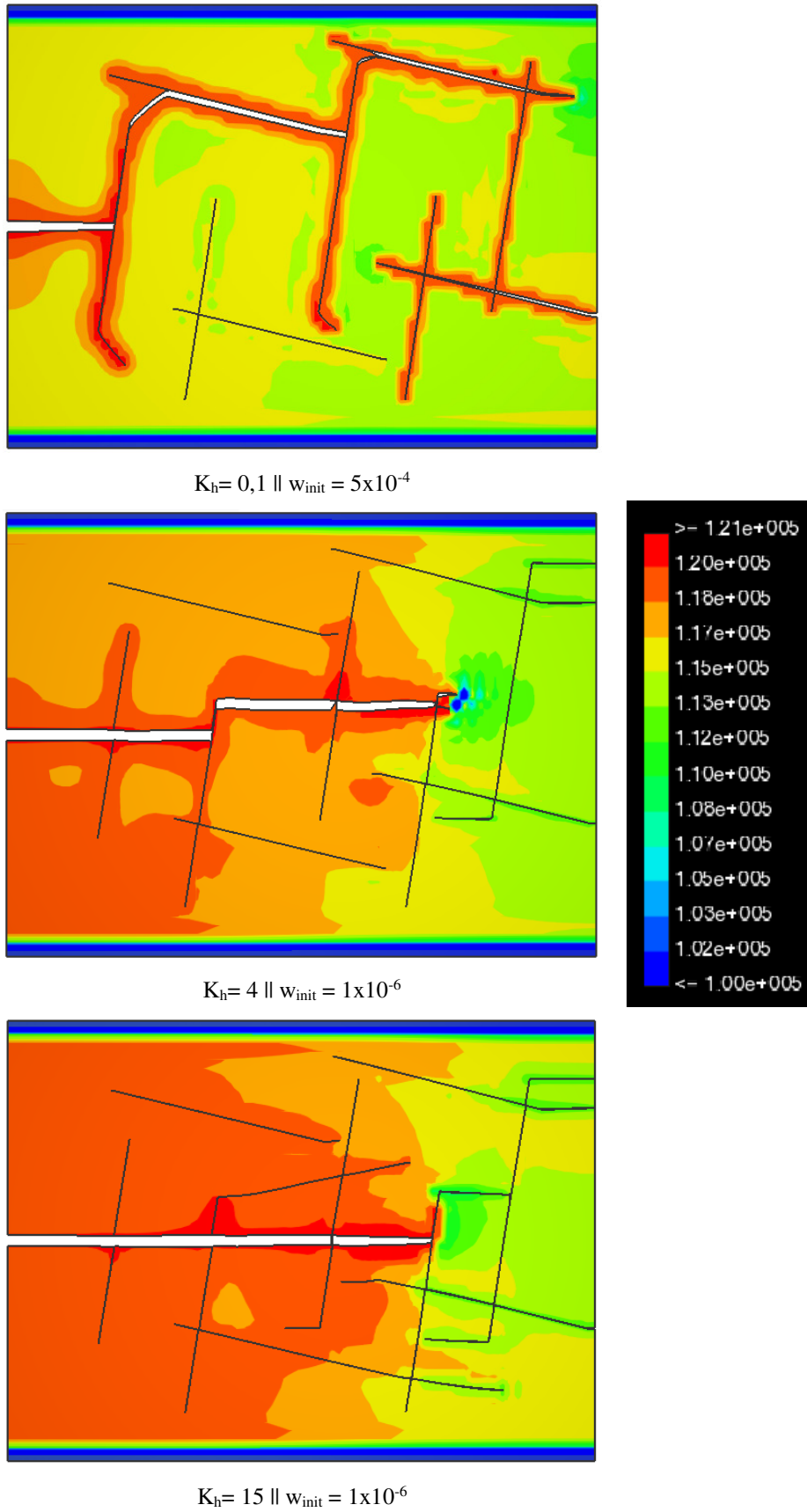


Figure 6.17 – Deformed models and pore-pressure fields at $t = 100$ s

In order to analyse the effect that the parameter variation has on the final fracture network pattern, Figure 6.18 shows the fracture networks for every computed simulation and highlights the propagated segments in blue. Different intersection types showed in previous examples are observed, namely crossing and opening. It is noticeable from all the deformed models that the natural fracture tips also propagate when their fluid pressure increases. It is also easily visible how higher differential stresses result in networks with more propagation segments. This is explained by the fact that, with a constant maximum in-situ stress in between simulations, a higher value of K_h is the result of a lower minimum in-situ stress, which consequently increases the possibility of propagation events.

For every simulation with very low differential stress parameters K_h at or near an isotropic state ($K_h = 0$ or $K_h = 0,1$), only opening events occur. As the parameter K_h increases, crossing becomes more and more predominant and the fracture network becomes more complex, increasing communication between natural fractures.

Comparisons of results for equal in-situ stress states show that for a very low in-situ hydraulic aperture (1×10^{-6} m) crossing events tend to happen more often. This may be explained by the difficulty of the fluid to enter natural fractures. For high and intermediate fracture apertures, 5×10^{-4} m and 5×10^{-5} m, respectively, the results are slightly similar.

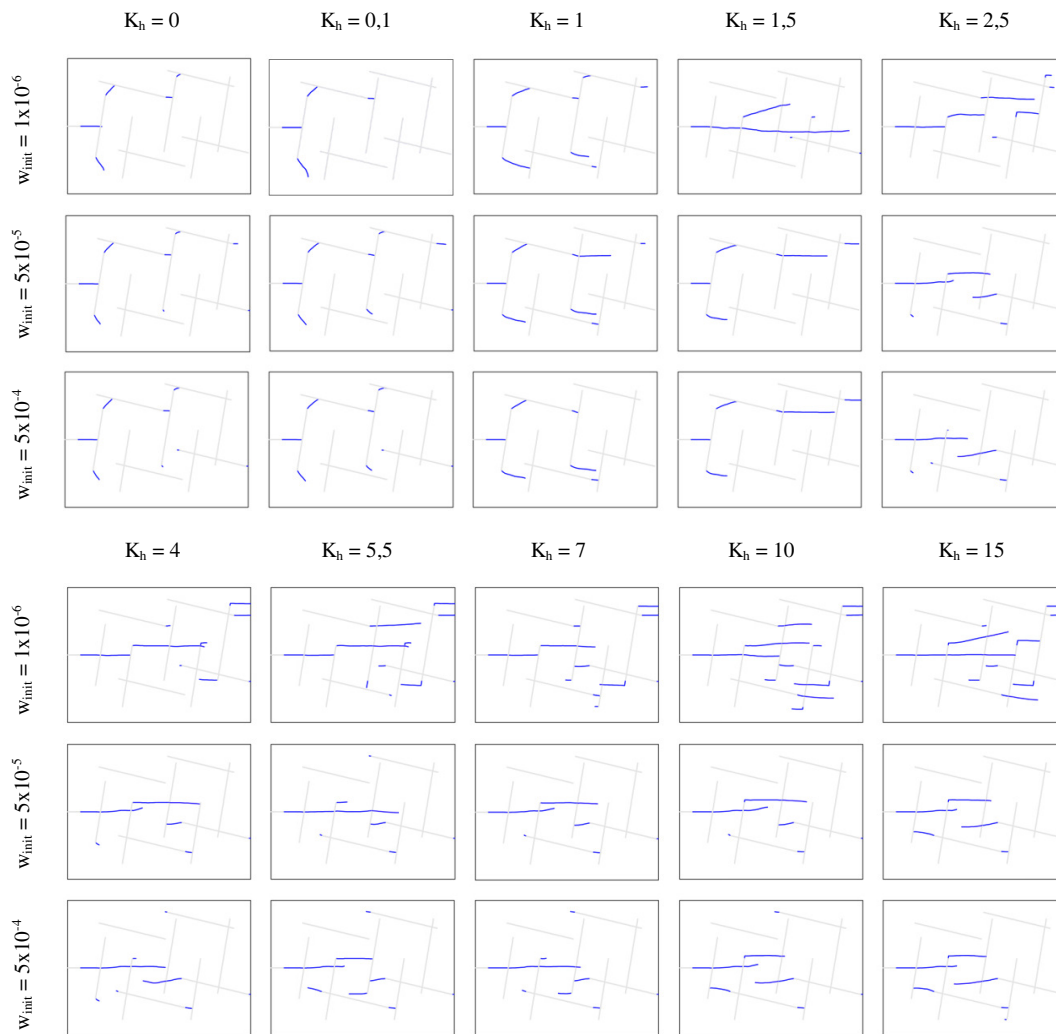


Figure 6.18 – Final fracture network ($t = 100$ s). Initial fractures in light grey and propagated segments in blue

Figure 6.19 complements the analysis of the results by showing the relative fracture aperture, i.e. the fracture aperture divided by the maximum fracture aperture in each simulation, at the end of the treatment. In this figure, it is visible that sub-horizontal fractures experience much larger apertures than the sub-vertical ones. This is expected, as the minimum in-situ stress acts in the vertical direction.

For values of K_h lower than 1, the fracture apertures tend to increase uniformly in the fracture network, indicating that the network grows in a more random manner, depending on the natural fracture position and not so much on the simulation parameters.

As the differential stress increases, the natural fractures aperture are much higher on the sub-horizontal fractures and the fracture network tends to develop

towards the preferred direction, i.e. the maximum in-situ-stress. For lower values of in-situ fracture aperture, this effect is even more evident.

The effect of stress shadowing between fractures is also noticeable in Figure 6.19. When the fracture network develops in parallel fractures (e.g. the simulation with $K_h = 7$ and $w_{init} = 5 \times 10^{-5}$), both fractures show a decrease in their aperture due to the compression effect between each other.

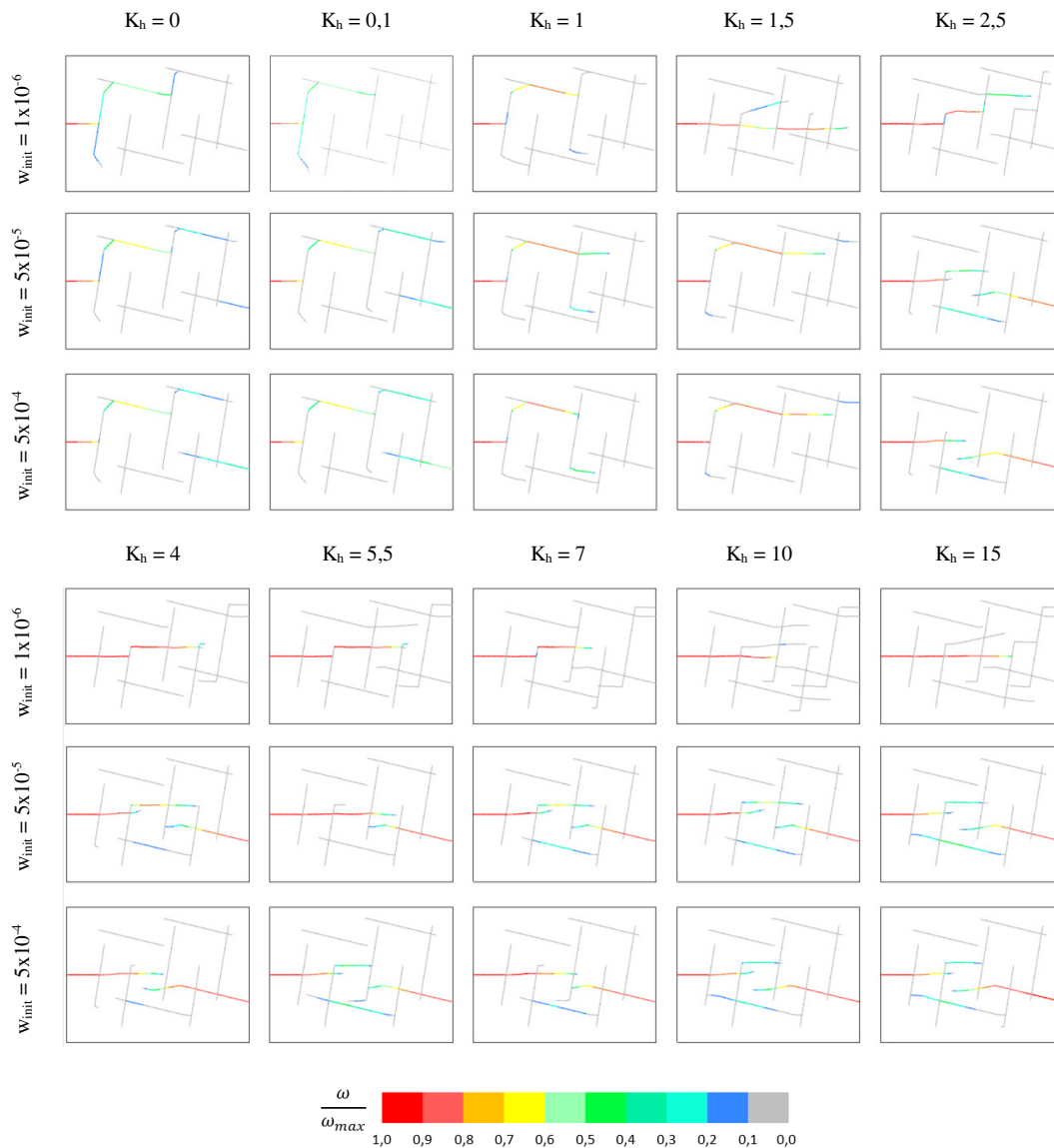


Figure 6.19 – Relative fracture opening in the final fracture network ($t = 100$ s).

Finally, a qualitative evaluation of the fracture pattern based in Figure 6.19 is plotted in Figure 6.20. Although being a very subjective analysis, three types of fracture network patterns are differentiated: random growth of fractures that is dependent on the initial fracture network, a partial horizontal hydraulic fracture

with multiple branches and a main horizontal hydraulic fracture with branches. It is concluded that high values of differential in-situ stress result in propagation of the hydraulic fracture in the preferred direction, while the in-situ fracture aperture may influence the flow of injection fluid into the natural fractures. For lower values of differential in-situ stress, the final fracture network tends to be similar to the initial one.

Even considering that it is not the object of this chapter to simulate a real laboratory test, the resulting plot of Figure 6.20 may be compared with the plot presented by Zhou and Xue (2011) (see Figure 6.14). Though many aspects of the simulation, such as rock parameters, boundary conditions and model geometry, are not the same, a similar behaviour may be interpreted from both numerical and laboratory results.

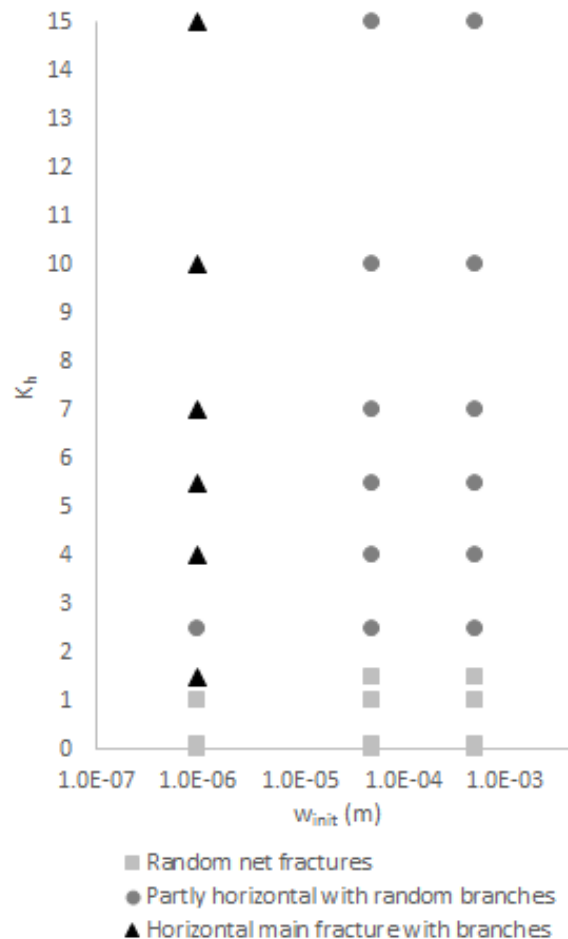


Figure 6.20 – Description of the final fracture network pattern ($t = 100$ s).

6.3. Percolation through a dam foundation

General description of the simulation

The main objective of this simulation is to demonstrate that the implemented code can be applied to simulate engineering problems other than intersection between hydraulic and natural fractures. The explicit consideration of fractures and their longitudinal and transversal flow is essential in many problems in rock foundations or reservoir geomechanics. In this simulation, the percolation through a fractured dam foundation is analysed in two sets of calculations.

In the first set, a foundation with one family of fractures equally spaced is subjected to a variation of the parameters that influence fractures longitudinal and transversal permeabilities. The models are based in the work by Segura and Carol (2004), as seen in Figure 6.21, and results are compared to the ones presented by the authors. The authors used and compared three types of interface elements – one, two and three nodes in the transversal direction. In this chapter, the current implementation is compared with the solutions of the models where the element with three nodes in the transversal direction was used.

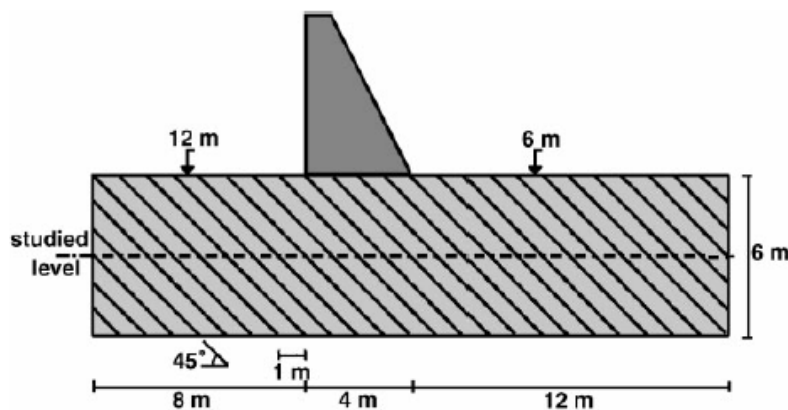


Figure 6.21 – Schematic model used by (Segura and Carol, 2004)

In the second set of calculations, a second family of fractures is introduced and its influence is analysed. All the performed calculations consider only the variables of the hydraulic part, i.e. the pore-pressures and the fracture fluid pressures.

Model geometry and mesh

Four different geometries – Dam0, Dam1, Dam2, Dam3 – were defined to perform the analyses and are presented in Figure 6.22. The first geometry (Dam0) is for the benchmark analysis of a homogeneous medium without fractures. Dam1, which is used in the first set of calculations, has 29 fractures equally spaced $\sqrt{2}$ m with inclination angle of 45° . For the second set of calculations, the geometries Dam2 and Dam3 are used. In the geometry Dam2 one fracture with inclination of 10° is introduced and in model Dam3 this fracture is replicated with a spacing of 1,5 m.

Both Dam0 and Dam1 have a 15 x 60 quadrilateral element regular mesh, while Dam2 and Dam3 have more refined meshes with 30 x 120 elements. Although a pre-study revealed that the coarser mesh provides results with sufficient quality, the existence of more fractures demands the use of a finer mesh to avoid the repetition of the same degree of freedom for different fractures in the same element (explained in Chapter 4.2.8).

Material properties

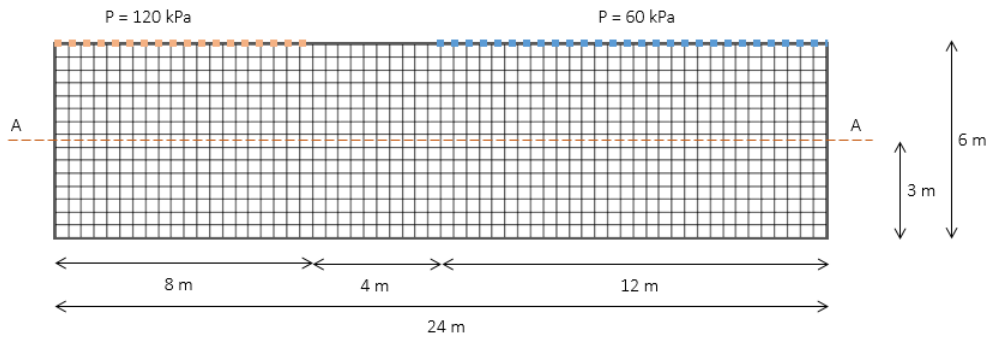
The parameters chosen for both the porous region and the fractures are presented from Table 6.10 to Table 6.12. Given the relation between hydraulic head h and hydraulic pressure p

$$p = h \times \gamma_w \quad (6.1)$$

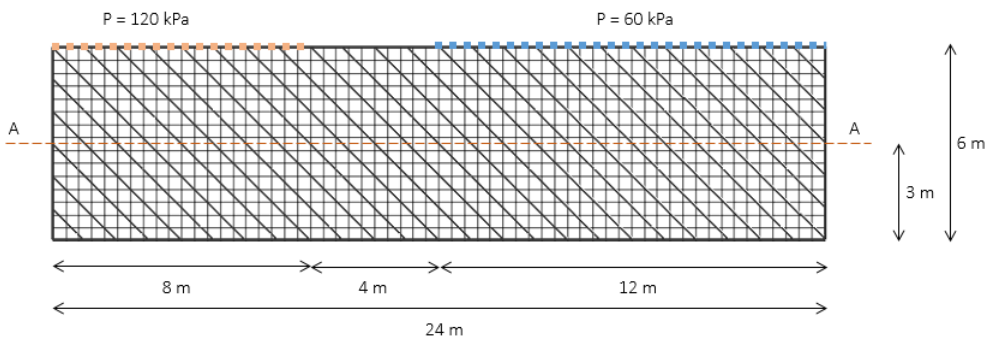
where γ_w is the water's volumetric weight, the flow rate and the transversal permeability in Segura and Carol (2004) may be presented as

$$q = k_t \Delta h = \frac{k_t}{\gamma_w} \Delta p \quad (6.2)$$

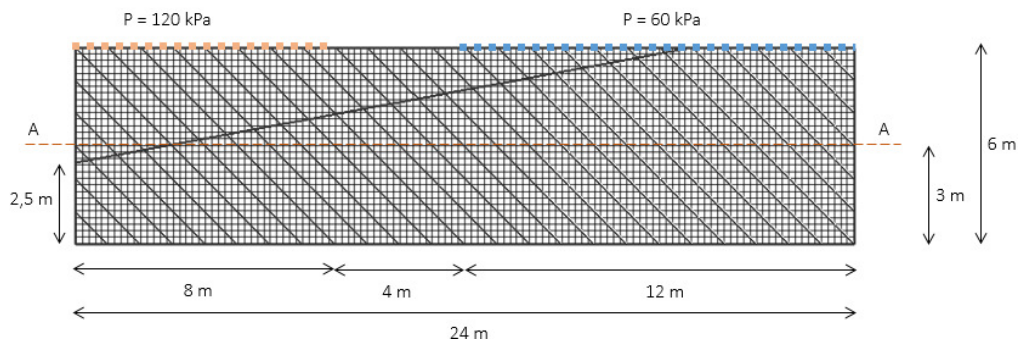
where the conductivity term k_t/γ_w (units $[1/T]/[F/L^3]$) may be defined to be equal to the fracture face transversal conductivity as implemented in this research (units $[L/T]/[F/L^2]$).



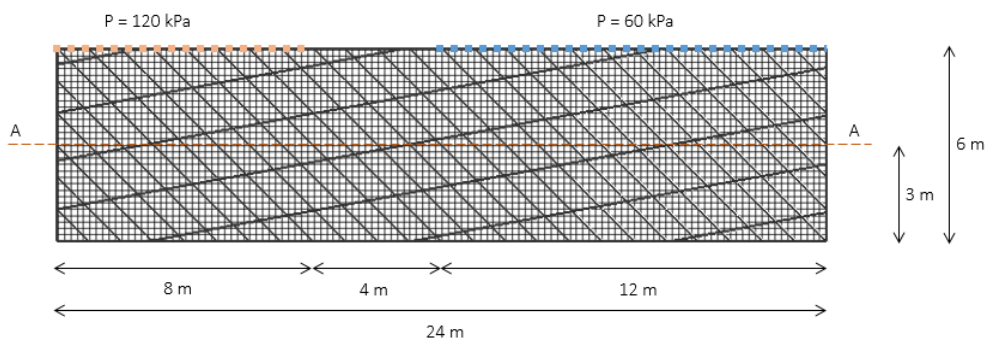
a)



b)



c)



d)

**Figure 6.22 – Geometry and boundary conditions for the models:
a) Dam0. b) Dam1. c) Dam2. d) Dam3**

Table 6.10 – Hydraulic properties

	Parameter	Dam0	Dam1	Dam2	Dam3
Porous Region	Hydraulic conductivity: $k = k_x = k_y$ (m/s)	10^{-7}			
Fractures	Hydraulic aperture: w_{init} (m)	-	See Table 6.11	See Table 6.12	
	Fracture face transversal conductivity: $c = c_{top} = c_{bottom}$ (m/s.kPa ⁻¹)	-		10^{-5}	
	Fluid Viscosity (kPa.s)	10^{-6}			

In the first set of calculations, the fracture hydraulic parameters – fracture hydraulic aperture and fracture face transversal conductivity – vary according to the analyses performed by Segura and Carol (2004). Table 6.11 presents the values used in every calculation.

In the second set of calculations, a second family of fractures is introduced. The fracture properties vary so the influence of the second set of fractures may be understood. To reduce the complexity of the analysis, only the hydraulic aperture varies, while the fracture face transversal conductivity is kept constant with a value of 10^{-5} m/s.kPa⁻¹. This value was chosen sufficiently high so that the transversal conductivity would not affect the results. The values of the hydraulic aperture for each calculation is presented in Table 6.12.

Table 6.11 – Hydraulic properties of fractures in the first set of calculations

Model	w_{init} (m)	c (m/s.kPa ⁻¹)
Dam1a	1×10^{-4}	10^{-5}
Dam1b	1×10^{-4}	10^{-8}
Dam1c	1×10^{-4}	10^{-9}
Dam1d	5×10^{-5}	10^{-5}
Dam1e	5×10^{-5}	10^{-8}
Dam1f	5×10^{-5}	10^{-9}
Dam1g	1×10^{-5}	10^{-5}
Dam1h	1×10^{-5}	10^{-8}
Dam1i	1×10^{-5}	10^{-9}

Table 6.12 – Hydraulic properties of fractures in the second set of calculations

Model	Fracture family	w_{init} (m)
Dam2a	45°	1×10^{-4}
	10°	1×10^{-4}
Dam2b	45°	1×10^{-4}
	10°	1×10^{-3}
Dam3a	45°	1×10^{-4}
	10°	1×10^{-4}
Dam3b	45°	1×10^{-4}
	10°	1×10^{-3}
Dam3c	45°	1×10^{-3}
	10°	1×10^{-4}

Boundary and loading conditions

As seen in Figure 6.22, the boundary conditions were set equally to every calculation. The effect of the water levels of 12 m and 6 m is introduced as imposed

pressures in the boundaries of 120 kPa and 60 kPa, respectively. All calculations are performed in a single increment, assuming that a permanent regime exists.

Results – Set 1 of Calculations – Comparison with Segura and Carol (2004)

The pore-pressure shadings for all the models with geometry Dam1 (1 set of fractures) are presented in Figure 6.23, together with the values of fracture face transversal conductivity and hydraulic aperture used in each calculation. It may be easily observed that the pore-pressure field changes considerable between each calculation.

For the calculations with the lowest fracture face transversal conductivity (leftmost column – $1 \times 10^{-9} \text{ m/s.kPa}^{-1}$), the fractures work as barriers to the fluid flow, retaining values of similar pressure in each space between fractures. With the increase in the transversal conductivity (middle and rightmost columns – 1×10^{-8} and $1 \times 10^{-5} \text{ m/s.kPa}^{-1}$), the percolation occurs with less loss of energy and this “barrier effect” vanishes.

As for the longitudinal transmissibility, which is directly related with the fracture aperture, it is noticeable that a lower conductivity (upper row – $1 \times 10^{-5} \text{ m}$) results in a more distributed pressure field. Higher apertures (middle and lower rows – 5×10^{-5} and $1 \times 10^{-4} \text{ m}$) facilitate the use of the fractures as canals for the fluid percolation. This leads to a concentration of pressure gradients in the middle of the model, which is the region where the fluid needs to leave the fractures and cross the less permeable porous medium.

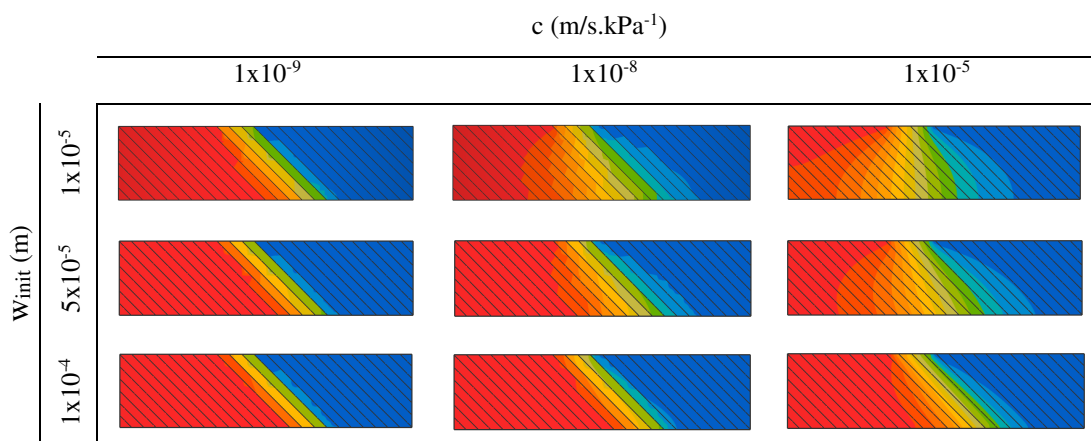


Figure 6.23 – Resulting pore pressures in models Dam1a to Dam1i (colour scale: red is 120 kPa, blue is 60 kPa)

From the analysis of Figure 6.24, it may be observed how the volume of fluid that enters (or leaves) the model decreases with the decrease of both longitudinal and transversal conductivity, as expected. In the cases with high values of fracture face transversal conductivity, the results almost match the ones presented by Segura and Carol (2004). As the fracture transversal flow decreases, the relative error between methods increases. The same assumptions may be made from observation of Figure 6.25. The pore-pressures along section A-A match for the models with high fracture face transversal conductivity, while a slight error is observable in the cases with lower values.

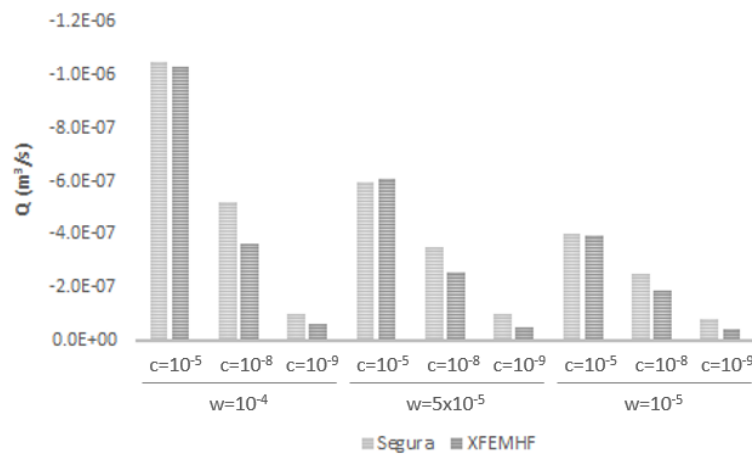
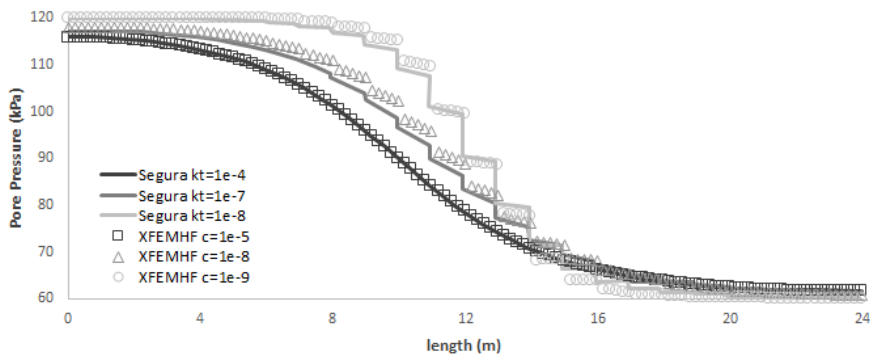
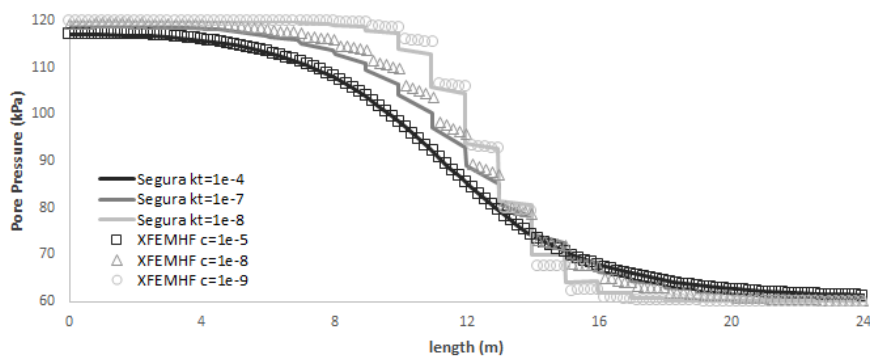


Figure 6.24 – Volumetric flow rate in models Dam1a to Dam1c

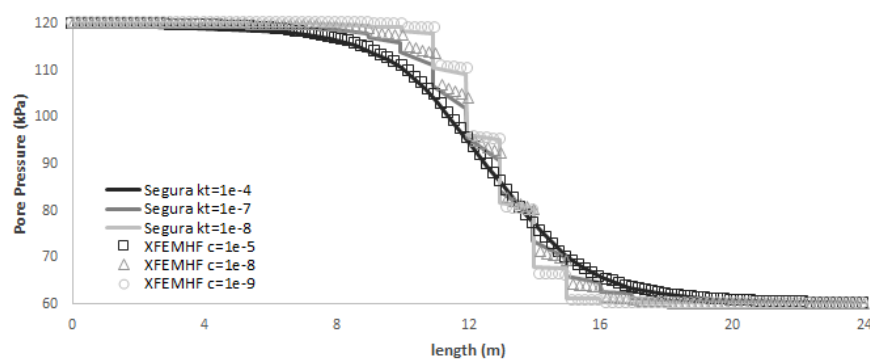
Although the comparison is made between different types of elements, it may be stated that the results show good agreement. It must be highlighted that the results from Segura and Carol (2004) were taken from printed plots, which may explain some of the differences. Other reasons may be the type mesh used by the authors and the way boundary conditions are applied, which were not detailed in the paper.



a)



b)



c)

Figure 6.25 – Pore Pressure values in section A-A. a) Models Dam1a, Dam1b and Dam1c – $w_{init}=10^{-4}$ m. b) Models Dam1d, Dam1e and Dam1f – $w_{init}=5 \times 10^{-5}$ m. c) Models Dam1g, Dam1h and Dam1i – $w_{init}=10^{-5}$ m.

Results – Set 2 of Calculations

In the second set of calculations, more fractures are introduced and higher fracture longitudinal permeabilities are used, so their effect is quantified. The values of the volumetric flow rates are presented in Figure 6.26 for comparison between models and the model Dam0 (without fractures) is used as benchmark. As seen in

Figure 6.27, the pore pressures field in model Dam0 shows a wide gradient of pore pressures along the model, with volumetric fluxes of the same order of magnitude of model Dam1a. As a new fracture is introduced with the same longitudinal transmissibility (model Dam2a), the volumetric fluxes increase as expected, as well as the pore-pressure gradients are more concentrated. However, with the increase of the longitudinal transmissibility of that single fracture (model Dam2b) a change of magnitude order of the volumetric flux is observed. It is also noticeable from Figure 6.28 that the gradient in the porous mediums reduces drastically, as almost all the pressure dissipates when the 10° fracture is reached. As expected, the increase of longitudinal transmissibility of this fracture creates a “canal” for the fluid to flow directly to the outer boundary.

The models Dam3a, Dam3b and Dam3c show that the hydraulic aperture and fracture position have much more influence in the flow than the number of fractures itself. As seen in Figure 6.29 together with Figure 6.26, the existing of a second set of fractures with the same longitudinal transmissibility increases the volumetric fluxes in a low level (model dam3a). However, an increase in the longitudinal transmissibility, as in models Dam3b and Dam3c, considerably increases the volumetric fluxes and changes the pore pressure gradients. The differences between models Dam3b and Dam3c show that the geometrical position of each set of fractures strongly influences the results, i.e. the increasing of longitudinal transmissibility is much more effective in fractures that are in a position that create paths for the fluid to flow easily. This is also supported if the fluxes and pore pressure fields of models Dam2b and Dam3b are compared. Despite the increasing in the volumetric fluxes, the presence of more fractures does not change the pore pressure fields considerably, as the single fracture of model Dam2b is the only fracture in model Dam3b that reaches directly the outer boundary of the model.

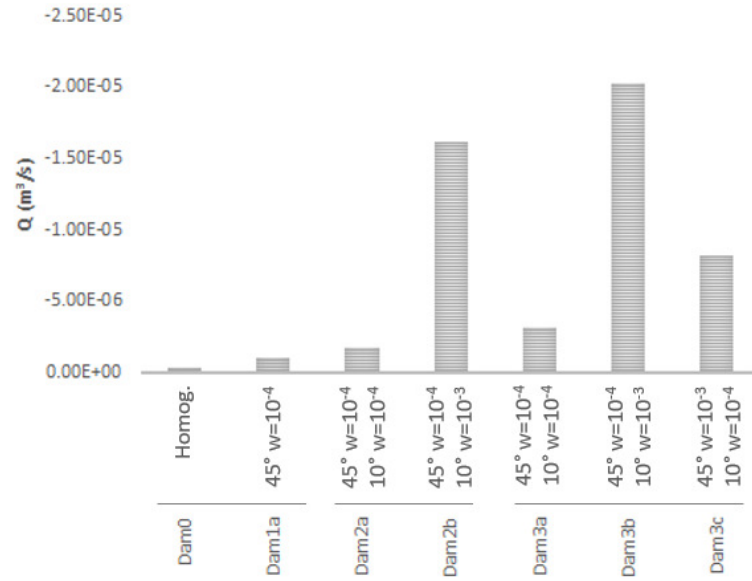
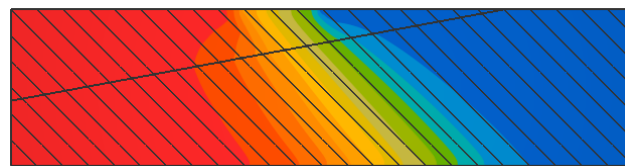


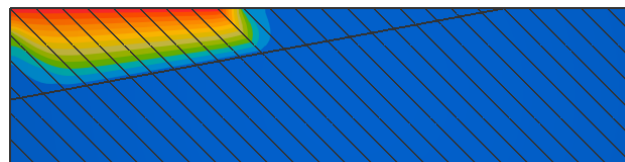
Figure 6.26 – Volumetric flow rate in models Dam0, Dam1a, Dam2a, Dam2b, Dam3a, Dam3b and Dam 3c



Figure 6.27 – Pore Pressure values for model Dam0 (colour scale: red is 120 kPa, blue is 60 kPa)

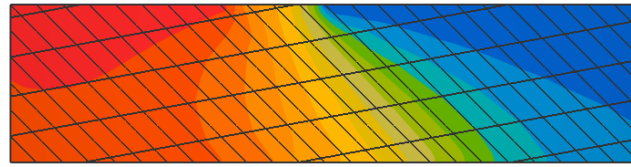


Dam2a (45° $w_{init} = 1 \times 10^{-4}$, 10° $w_{init} = 1 \times 10^{-4}$)

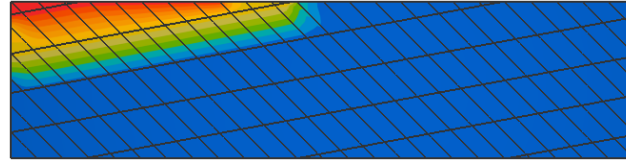


Dam2b (45° $w_{init} = 1 \times 10^{-4}$, 10° $w_{init} = 1 \times 10^{-3}$)

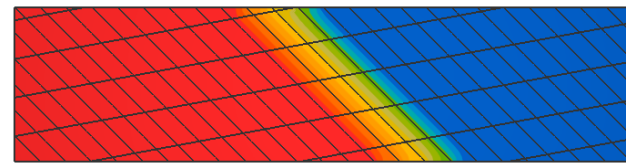
Figure 6.28 – Pore Pressure values for models Dam2a and Dam 2b (colour scale: red is 120 kPa, blue is 60 kPa)



Dam3a ($45^\circ w_{init} = 1 \times 10^{-4}$, $10^\circ w_{init} = 1 \times 10^{-4}$)



Dam3b ($45^\circ w_{init} = 1 \times 10^{-4}$, $10^\circ w_{init} = 1 \times 10^{-3}$)



Dam3c ($45^\circ w_{init} = 1 \times 10^{-3}$, $10^\circ w_{init} = 1 \times 10^{-4}$)

Figure 6.29 – Pore Pressure values for models Dam3a, Dam3b and Dam3c (colour scale: red is 120 kPa, blue is 60 kPa)